AUTOPHAGY
2020, VOL. 16, NO. 9, 1598–1617
https://doi.org/10.1080/15548627.2019.1695398

Taylor & Francis
Taylor & Francis Group

RESEARCH PAPER

CASP9 (caspase 9) is essential for autophagosome maturation through regulation of mitochondrial homeostasis

Hyun-Kyu An[a], Kyung Min Chung[a], Hyunhee Park[a], Jihyun Hong[a], Ji-Eun Gim[a], Hyosun Choi[b], Ye Won Lee[a], Jieun Choi[a], Ji Young Mun [c], and Seong-Woon Yu[a,d]

[a]Department of Brain and Cognitive Sciences, Daegu Gyeongbuk Institute of Science and Technology, Daegu, Republic of Korea; [b]BK21 Plus Program, Department of Senior Healthcare, Graduate School, Eulji University, Daejeon, Republic of Korea; [c]Department of Structure and Function of Neural Network, Korea Brain Research Institute, Daegu, Republic of Korea; [d]Neurometabolomics Research Center, Daegu Gyeongbuk Institute of Science and Technology (DGIST), Daegu, Republic of Korea

ABSTRACT

CASP9 (caspase 9) is a well-known initiator caspase which triggers intrinsic apoptosis. Recent studies also suggest various non-apoptotic roles of CASP9, including macroautophagy/autophagy regulation. However, the involvement of CASP9 in autophagy and its molecular mechanisms are not well understood. Here we report the non-apoptotic function of CASP9 in positive regulation of autophagy through maintenance of mitochondrial homeostasis. Growth factor or amino acid deprivation-induced autophagy activated CASP9, but without apoptotic features. Pharmacological inhibition or genetic ablation of *CASP9* decreased autophagy flux, while ectopic expression of CASP9 rescued autophagy defects. In *CASP9* knockout (KO) cells, initiation and elongation of phagophore membranes were normal, but sealing of the membranes and autophagosome maturation were impaired, and the lifetime of autophagosomes was prolonged. Ablation of *CASP9* caused an accumulation of inactive ATG3 and decreased lipidation of the Atg8-family members, most severely that of GABARAPL1. Moreover, it resulted in abnormal mitochondrial morphology with depolarization of the membrane potential, reduced reactive oxygen species production, and aberrant accumulation of mitochondrial fusion-fission proteins. CASP9 expression or exogenously added H_2O_2 in the *CASP9* KO cells corrected the ATG3 level and lipidation status of Atg8-family members, and restored autophagy flux. Of note, only CASP9 expression but not H_2O_2 rescued mitochondrial defects, revealing regulation of mitochondrial homeostasis by CASP9. Our findings suggest a new regulatory link between mitochondria and autophagy through CASP9 activity, especially for the proper operation of the Atg8-family conjugation system and autophagosome closure and maturation.

Abbreviations: AA: amino acid; ACD: autophagic cell death; ACTB: actin beta; ANXA5: annexin A5; APAF1: apoptotic peptidase activating factor 1; Atg: autophagy related; ATG16L1: autophagy related 16 like 1; $BafA_1$: bafilomycin A_1; BCL2: BCL2 apoptosis regulator; BECN1: beclin 1; CARD: caspase recruitment domain containing; CASP: caspase; CM-H_2DCFDA: chloromethyl-2′,7′-dichlorodihydrofluorescein diacetate; Δψm: mitochondrial membrane potential; DN: dominant-negative; DNM1L/DRP1: dynamin 1 like; EBSS: Earle's balanced salt solution; GABARAP: GABA type A receptor-associated protein; GABARAPL1: GABA type A receptor associated protein like 1; GABARAPL2: GABA type A receptor associated protein like 2; HCN: hippocampal neural stem cells; IAM: inner autophagosome membrane; INS: insulin; KO: knockout; LEHD: Z-LEHD-fmk; MAP1LC3: microtubule associated protein 1 light chain 3; MFN1: mitofusin 1; MFN2: mitofusin 2; MTORC1: mechanistic target of rapamycin kinase complex 1; PARP1: poly(ADP-ribose) polymerase 1; PBS: phosphate-buffered saline; PE: phosphatidylethanolamine; ROS: reactive oxygen species; sgRNA: single guide RNA; SR-SIM: super-resolution structured illumination microscopy; SQSTM1: sequestosome 1; STS: staurosporine; STX17: syntaxin 17; TMRE: tetramethylrhodamine ethyl ester; TUBB: tubulin beta class I; ULK1: unc-51 like autophagy activating kinase 1; WT: wild type; ZFYVE1/DFCP1: zinc finger FYVE-type containing 1

ARTICLE HISTORY
Received 20 January 2019
Revised 30 October 2019
Accepted 7 November 2019

KEYWORDS
ATG3; autophagosome maturation; caspase 9; membrane closure; mitochondria; reactive oxygen species

Introduction

Macroautophagy (commonly referred to as autophagy) is a lysosome-dependent, intracellular self-digestion process which degrades various cytoplasmic materials as well as invading pathogens [1–4]. Autophagy is essential for cell survival in the presence of diverse stressors including nutrient or growth factor deprivation, and also plays a critical role in maintaining cellular homeostasis at the basal state by ensuring turnover of proteins, metabolites and organelles [1–4]. Autophagy is characterized by an increase in the number of autophagic vesicles (autophagosomes for sequestration and delivery of intracellular cargo materials, and autolysosomes for cargo degradation and recycling) [5]. Autophagosome biogenesis is a multi-stage process and begins by forming a nascent cup-shaped phagophore, which is followed by

CONTACT Seong-Woon Yu yusw@dgist.ac.kr Department of Brain and Cognitive Sciences, Daegu Gyeongbuk Institute of Science and Technology (DGIST), 333 Techno Jungang Daero, Hyeonpung-Myeon, Dalseong-Gun, Daegu 42988, Republic of Korea

This article has been republished with minor changes. These changes do not impact the academic content of the article.

elongation and closure of the phagophore membrane, resulting in a new double-membrane organelle, autophagosome. The autophagosome then fuses with a lysosome and matures into an autolysosome, where the inner autophagosome membrane (IAM) is degraded along with the cargos by lysosomal enzymes [6].

This complex process is tightly controlled by autophagy related (*ATG*) genes, especially by two ubiquitin-like conjugation systems involving ATG5, which is conjugated to ATG12 and forms an ATG12–ATG5-ATG16L1 complex, and Atg8-family proteins, which are conjugated to phosphatidylethanolamine (PE) [6]. There are two subfamilies of mammalian Atg8-family proteins: MAP1LC3/LC3 (microtubule associated protein 1 light chain 3), which includes MAP1LC3A, MAP1LC3B, MAP1LC3B2, and MAP1LC3C; and GABARAP (GABA type A receptor associated protein), which includes GABARAP, GABARAPL1 and GABARAPL2 [7]. Following the appearance of the nascent phagophore, these two conjugation systems expand and seal the membrane to generate an autophagosome. ATG7 serves as an E1-like enzyme for both ATG12 and Atg8-family proteins, and ATG10 and ATG3 as E2-like enzymes for ATG12 and Atg8-family proteins, respectively. Then, the ATG12–ATG5-ATG16L1 complex acts as an E3-like ligase to mediate PE-dependent lipidation of MAP1LC3 and GABARAP proteins; when lipidated, these are called MAP1LC3-II/GABARAP-II and associated with autophagosomes, whereas their cytosolic, nonconjugated forms are called MAP1LC3-I/GABARAP-I [6].

Autophagy and apoptosis are two key cellular processes for cell survival and death. Although there is a growing recognition of the sophisticated intersection of apoptotic and autophagic molecular networks, the mechanisms mediating their interaction are far from clear. They involve a set of multifunctional molecules that participate in both apoptosis and autophagy. The well-known molecules with dual roles in autophagy and apoptosis are BCL2 (BCL2 apoptosis regulator) and BECN1 (beclin 1) [8]. There is a growing list of other proteins with such dual roles. For example, ATG12 associates with anti-apoptotic BCL2 and MCL1, thereby promoting mitochondrial apoptosis [9]. Caspases (CASPs) are cysteine-dependent aspartate-specific proteases indispensable for apoptosis [10]. In addition, their functions in regulation of autophagy are also gaining attention. Association of CASPs with autophagy has been reported during starvation or developmental cell death in *Drosophila* [11,12]. A *Drosophila* CASP, Dcp-1, promotes autophagy by decreasing the levels of the mitochondrial protein SesB and ATP [13]. In mammalian cells, CASPs regulate autophagy in both positive and negative ways. Binding of CASP9 to ATG7 facilitates MAP1LC3B lipidation and autophagosome formation in a CASP9 activity-independent manner [14]. Inhibition of CASP9 suppresses autophagy flux and enhances cell death in MCF-7 cells, revealing CASP9 involvement in an autophagy-mediated survival pathway [15]. On the other hand, ablation of CASP8 enhances autophagy signaling and necroptotic cell death in proliferating T-cells, suggesting that CASP8 limits hyperactivation of autophagy and prevents autophagy from inducing T-cell death [16]. CASP2 negatively regulates autophagy, and loss of CASP2 leads to AMP-dependent protein kinase (AMPK) activation and reactive oxygen species (ROS) production in mouse embryonic fibroblasts [17]. Furthermore, various human ATG proteins are cleaved by CASPs, suggesting CASP-mediated inhibition of autophagy [18]. Conversely, autophagy can degrade CASPs to counterbalance apoptosis induction [19]. These findings suggest that the cross-talk between autophagy and apoptosis is important for cell fate determination by regulating the balance of cell survival and death.

We have previously reported that INS (insulin) withdrawal induces autophagic cell death (ACD) in adult rat hippocampal neural stem (HCN) cells, although they have fully functional apoptotic capability [20–23]. ACD, also called type II programmed cell death is defined as follows; i) autophagy flux is increased during cell death, ii) no involvement of apoptotic machinery, iii) blockage of cell death by suppression of autophagy genes [24–26]. The absence of apoptotic markers in INS-deprived HCN cells, including chromosomal DNA fragmentation, nuclear condensation, CASP3 activation, and cleavage of PARP1 (poly[ADP-ribose] polymerase 1) have been well documented in our previous studies [20–23].

In this study, we report that autophagy flux induced by growth factor deprivation or amino acid (AA) starvation depends on CASP9 activity, which regulates mitochondrial homeostasis and production of ROS for the efficient autophagosome maturation. Our study uncovers a mitochondria-mediated molecular mechanism by which CASP9 exerts non-apoptotic function in maintenance of mitochondrial homeostasis and facilitation of autophagy.

Results

CASP9 is required for autophagy in HCN and HeLa cells

In agreement with our previous studies, INS withdrawal increased the level of the lipidated form of MAP1LC3B (MAP1LC3B-II) and decreased that of SQSTM1/p62 alongside an increase in cell death (Figure 1A,B). Apoptosis was not induced, as suggested by the observations that INS-deprived HCN cells were barely stained with ANXA5 (annexin A5), in contrast to a dramatic increase in ANXA5 staining by staurosporine (STS) treatment (Figure 1C). Z-VAD-fmk, a broad-spectrum CASP inhibitor, did not reduce cell death (Figure 1D).

CASPs are the principal apoptotic proteases, but they were also reported to cooperate with autophagy in the developmental cell death of salivary glands in *Drosophila* [12]. Thus, we tested whether CASP activities are required for ACD of HCN cells by testing the effects of inhibitors of individual caspases. Although, similar to Z-VAD-fmk, inhibitors specific for CASP3, CASP6, and CASP8 had no effect on cell death, a CASP9 inhibitor, Z-LEHD-fmk (LEHD), significantly reduced death of INS-deprived HCN cells (Figure 1D). Therefore, we checked whether CASP9 was activated following INS withdrawal. Under INS withdrawal condition, the cleaved form of CASP9, but not of CASP3, was increased, suggesting activation of CASP9 without activation of the apoptosis effector CASP3 (Figure 1E). Moreover, CASP9 activity was significantly increased by INS withdrawal compared to control and was suppressed by LEHD (Figure 1F). On the other hand, CASP3 activity was not

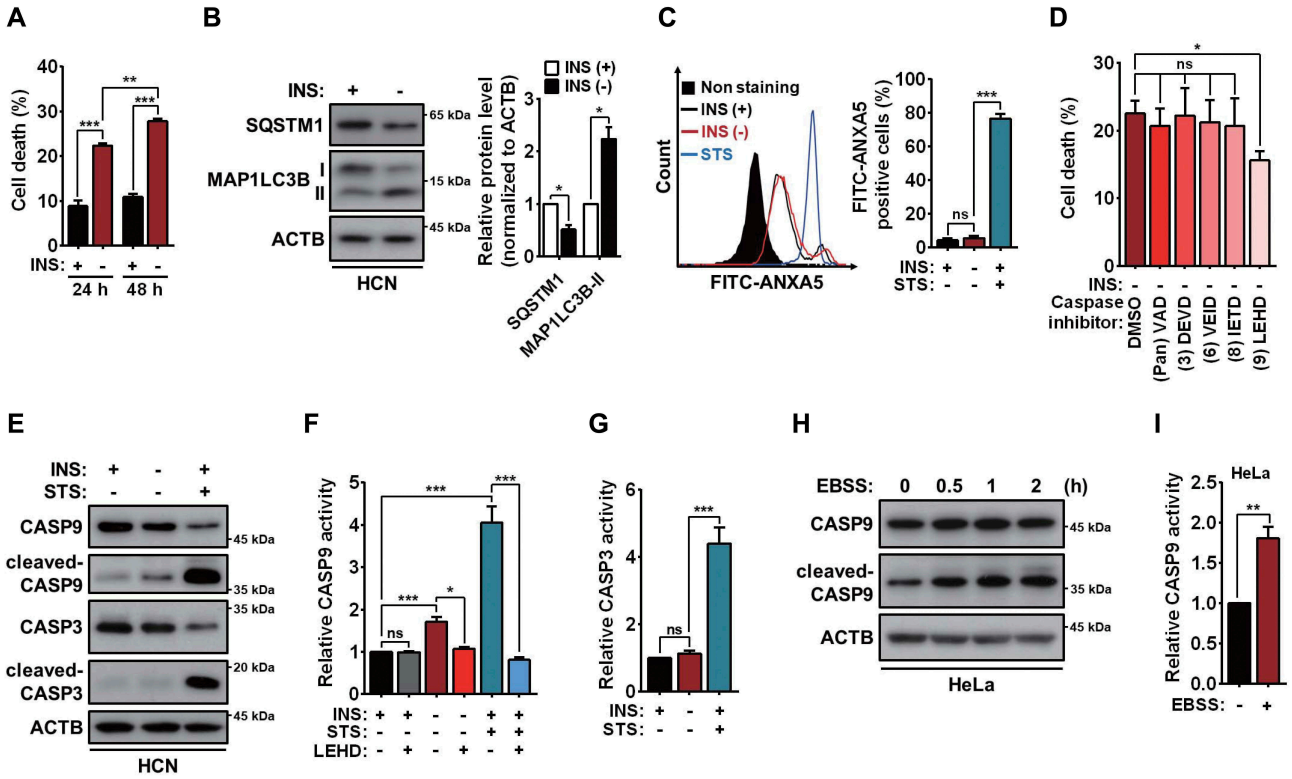

Figure 1. CASP9 is activated upon autophagy induction. (A) Cell death rate in HCN cells following INS withdrawal for 24 h and 48 h (n = 5). (B) Western blotting analysis of SQSTM1 and MAP1LC3B in HCN cells following INS withdrawal for 24 h. Graph, quantification of SQSTM1 and MAP1LC3B-II normalized to ACTB (n = 3). (C) Measurement of apoptosis by FITC-ANXA5 staining in HCN cells following INS withdrawal for 24 h. Staurosporine (STS, 0.5 μM for 12 h) was used as a positive control for apoptosis. Graph, quantification of FITC-ANXA5-positive cells (n = 5). (D) Cell death rate in HCN cells following INS withdrawal for 24 h without or with CASP inhibitors (20 μM each) (n = 3). (E) Western blotting analysis of CASP9 and CASP3 cleavage in HCN cells following INS withdrawal for 6 h. STS (0.5 μM, 3 h) was used as a positive control for CASP cleavage. The blots shown are representative of 3 experiments with similar results. (F) CASP9 activity in HCN cells after INS withdrawal or STS (0.25 μM) treatment for 4 h without or with LEHD (20 μM) (n = 5). (G) CASP3 activity in HCN cells after INS withdrawal or STS treatment (0.25 μM) for 4 h (n = 3). (H) Western blotting analysis of CASP9 cleavage in HeLa cells after AA starvation (EBSS) for the indicated time periods. The blots shown are representative of 3 experiments with similar results. (I) CASP9 activity in HeLa cells after AA starvation for 2 h (n = 3). *$P < 0.05$, **$P < 0.01$, and ***$P < 0.001$; ns, not significant.

increased by INS withdrawal (Figure 1G). Next, we checked whether CASP9 activation during autophagy occurs in other type of cell. In HeLa cells, AA starvation increased both cleavage and activity of CASP9 compared to the normal complete medium (Figure 1H,I). These results strongly suggest that CASP9 is activated during autophagy induction by growth factor deprivation or nutrient starvation.

Pharmacological inhibition of CASP9 suppresses autophagy flux

After we observed CASP9 activation during autophagy induction, we checked whether pharmacological inhibition of CASP9 would affect autophagy flux. We blocked the autophagosome–lysosome fusion with bafilomycin A_1 ($BafA_1$) and monitored autophagy flux by using two well-established methods [25]: western blotting analysis of MAP1LC3B-II amount and puncta counting using tandem monomeric RFP-GFP tagged MAP1LC3B (mRFP-GFP-MAP1LC3B). LEHD treatment significantly reduced the accumulated amount of MAP1LC3B-II when fusion was blocked in INS-deprived HCN cells (Figure 2A). Interestingly, LEHD treatment also slowed down MAP1LC3B turnover in the presence of INS (Figure 2A).

For the morphological analysis of autophagic organelles, we used HeLa cells, since they have a larger volume of cytoplasm with well-spread morphology, and have been widely used as an *in vitro* model for autophagy study. AA starvation induced similar total numbers of autophagic vesicles in both vehicle- and LEHD-treated HeLa cells transfected with the mRFP-GFP-MAP1LC3B plasmid (Figure 2B). However, maturation of autophagosomes into autolysosomes, detected as RFP-only puncta, was significantly decreased by LEHD treatment (Figure 2B). These results suggest that inhibition of CASP9 activity decreases autophagy flux by affecting autophagosome maturation rather than initiation of autophagosome biogenesis.

Knockout of CASP9 decreases autophagy flux

To corroborate these results derived from the pharmacological inhibition of CASP9, we generated *CASP9* KO cells using the CRISPR-Cas9 genome editing technique in both HCN and HeLa cells, and designated them sg*Casp9* (HCN cells) or sg*CASP9* (HeLa cells), with control cells designated sgCon. *CASP9* KO was confirmed by western blotting analysis

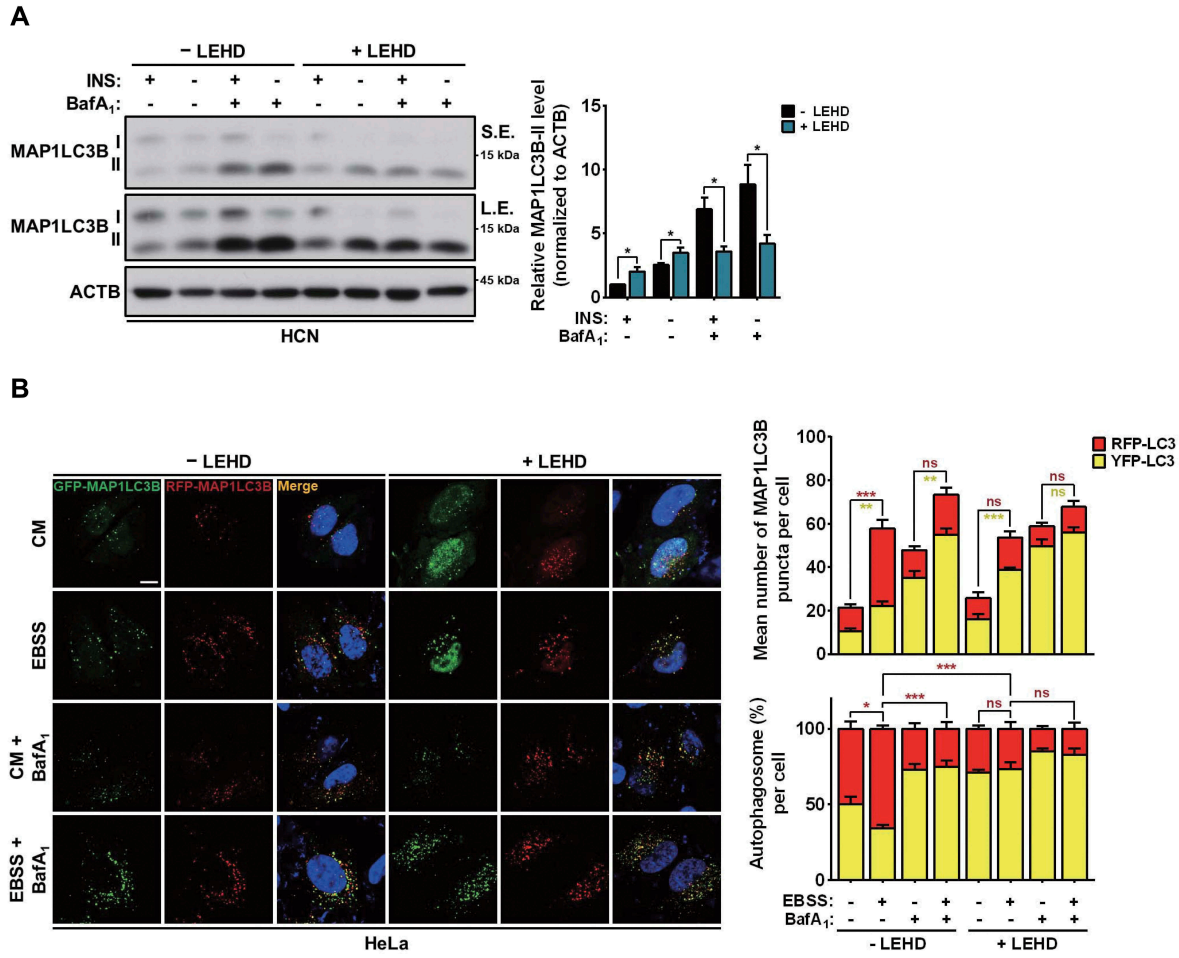

Figure 2. Pharmacological inhibition of CASP9 impairs autophagy flux. (A) Western blotting analysis of MAP1LC3B lipidation in HCN cells after INS withdrawal for 6 h without or with LEHD treatment (20 μM). $BafA_1$ (10 nM) was added 1 h before cell harvest. S. E., short exposure; L. E., long exposure. Graph, quantification of MAP1LC3B-II normalized to ACTB (n = 3). *$P < 0.05$. (B) Measurement of autophagy flux by mRFP-GFP-MAP1LC3B puncta assay in HeLa cells after AA starvation (EBSS, 1 h) without or with LEHD treatment (20 μM). $BafA_1$ (100 nM) was present during AA starvation. Graph, quantification of mRFP-GFP-MAP1LC3B puncta (n = 10 cells per each condition). Scale bar: 10 μm. *$P < 0.05$ and ***$P < 0.001$; ns, not significant for red MAP1LC3B puncta. *$P < 0.05$, **$P < 0.01$, and ***$P < 0.001$; ns, not significant for yellow MAP1LC3B puncta.

(Figure 3A,D). As expected, *CASP9* KO substantially attenuated CASP3 activation and PARP1 cleavage in STS-treated sg*Casp9* cells (Figure 3B). Introduction of wild type (WT) rat *Casp9* (*RnCasp9*) into sg*Casp9* cells restored CASP3 activation and PARP1 cleavage following STS treatment (Figure 3C).

There is a single isoform of CASP9 in rat, but 4 alternatively spliced variants in humans. Isoform 1 is an entire proform of CASP9. Isoform 2 has a caspase recruitment domain containing (CARD) and a small but not large catalytic domain, whereas isoform 3 has CARD only [27]. Isoforms 2 and 3 seem to play a role as endogenous inhibitors of apoptosis [28]. Isoform 4 has large and small catalytic domains, but no CARD (Figure 3E) and was predicted from human genome sequencing [29]. However, isoform 4 has not been cloned and its function remains to be elucidated. Single guide RNA (sgRNA) targeting of a sequence within CARD can ablate human CASP9 isoforms 1, 2, and 3, but not 4 (Figure 3E,F). To rule out the potential contribution of isoform 4 into CASP9 activity, we measured CASP9 activity following AA starvation in sgCon and sg*CASP9* cells. In sg*CASP9* cells, basal CASP9 activity was already lower than in sgCon cells, and AA starvation failed to increase it, suggesting that isoform 4 is not involved in regulation of CASP9 activation following starvation (Figure 3G).

Next, we examined the role of CASP9 in autophagy in *CASP9* KO cells. In agreement with the data obtained with LEHD treatment, *CASP9* KO significantly decreased the number of RFP-only autolysosomes, but not the total number of autophagic vesicles, following AA starvation in HeLa cells (Figure 4A). Additionally, western blotting analysis revealed decreased lipidation of MAP1LC3B both in *CASP9* KO HCN and HeLa cells (Figure 4B,C). In sg*Casp9* cells, CASP9 activity was dramatically decreased compared to sgCon cells at basal state and was not increased by INS withdrawal (Figure 4D). To confirm that the impaired autophagy flux in sg*Casp9* cells was due to the lack of CASP9 and determine whether CASP9 is sufficient to induce autophagy flux, we introduced *RnCasp9* WT or its catalytically inactive mutant form (C325A) into sg*Casp9* cells. Introduction of *RnCasp9* WT restored CASP9 activity and recovered autophagy flux following INS withdrawal (Figure 4E,F). In contrast, expression of the C325A mutant restored neither CASP9 activity nor autophagy flux (Figure 4E,F). These results suggest that defective

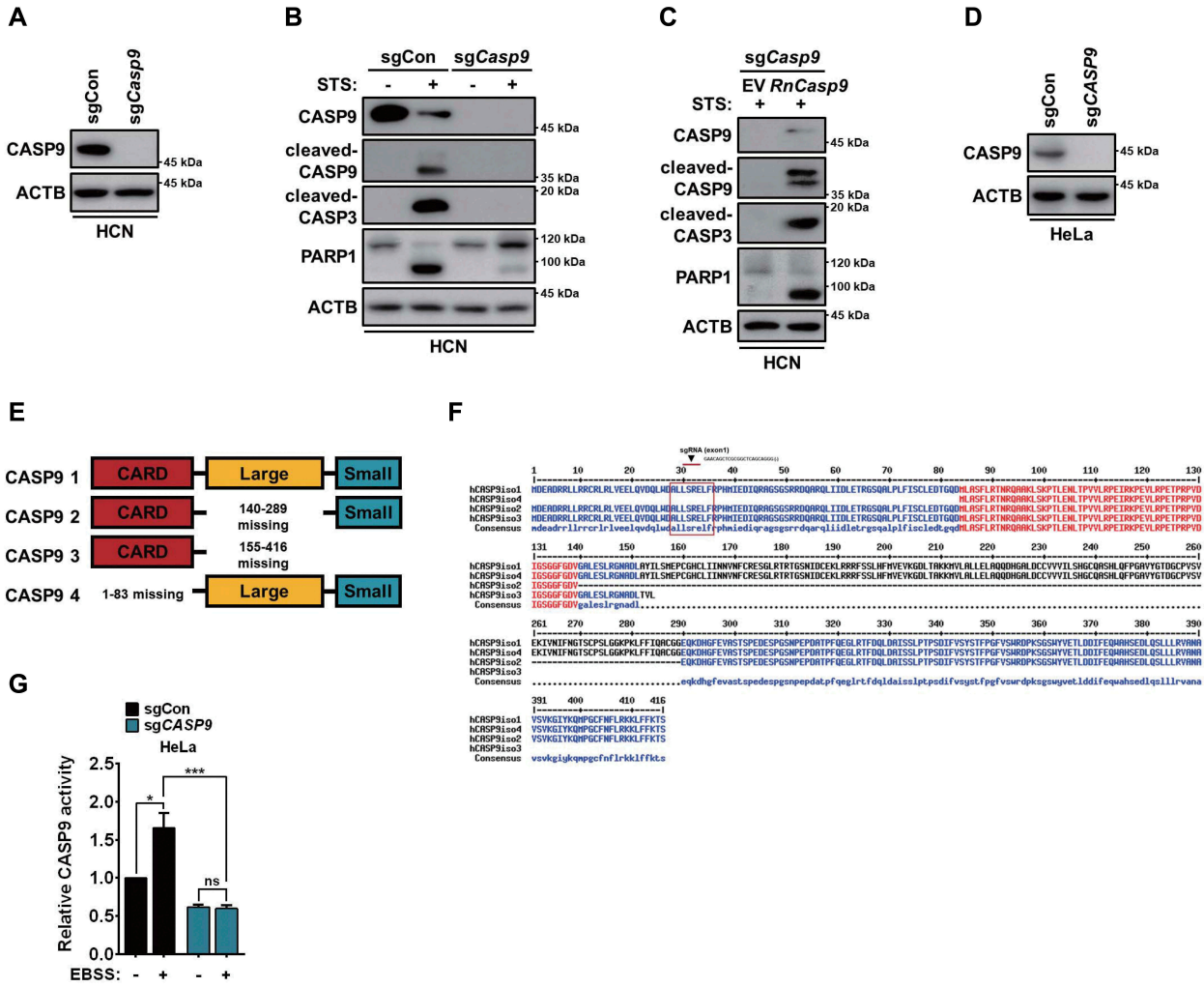

Figure 3. *CASP9* KO cells are resistant to STS-induced apoptosis. (A) Western blotting analysis for validation of *CASP9* KO in HCN cells. (B) Western blotting analysis of cleavage of CASP9, CASP3, and PARP1 in *CASP9* KO (sg*Casp9*) and control (sgCon) HCN cells after treatment with STS (0.5 μM, 3 h). The blots shown are representative of 3 experiments with similar results. (C) Western blotting analysis of cleavage of CASP9, CASP3, and PARP1 after treatment with STS (0.5 μM, 3 h) in sg*Casp9* HCN cells transfected with empty vector (EV) or wild-type (WT) rat *Casp9* (*RnCasp9*). The blots shown are representative of 3 experiments with similar results. (D) Western blotting analysis for validation of *CASP9* KO in HeLa cells. (E) Schematic diagram of isoforms of human CASP9. (F) sgRNA sequence used for generation of *CASP9* KO is marked as a red box. (G) CASP9 activity in sgCon and sg*CASP9* HeLa cells after AA starvation for 2 h (n = 3). *$P < 0.05$, ***$P < 0.001$; ns, not significant.

autophagy flux is caused by the loss of CASP9 function and the catalytic activity of CASP9 is critical for its ability to regulate autophagy.

APAF1 (apoptotic peptidase activating factor 1) is not required for autophagy flux

APAF1 is a well-known upstream molecule for CASP9 activation during apoptosis [30,31]. To check whether APAF1 is also involved in CASP9 activation during autophagy, we generated *APAF1* KO (sg*Apaf1*) HCN cells using the CRISPR-Cas9 system and validated the KO by western blotting analysis (Figure 5A). Attenuation of apoptosis in sg*Apaf1* cells following STS treatment was confirmed by the suppressed cleavage of CASP9 (Figure 5B). On the other hand, CASP9 activity in sg*Apaf1* HCN cells and in sgCon cells was increased similarly (1.62 ± 0.08 *vs* 1.7 ± 0.05 fold) following INS withdrawal, although basal CASP9 activity was lower in sg*Apaf1* than in sgCon cells (Figure 5C). Furthermore, both sgCon and sg*Apaf1* HCN cells showed the same level of MAP1LC3B lipidation induced by INS withdrawal (Figure 5D). These results indicate that APAF1 is involved neither in autophagy-induced CASP9 activation nor in autophagy flux in HCN cells following INS withdrawal. Consistent with these results of CASP9 activation and autophagy flux, sg*Apaf1* cells were resistant to STS, but not to INS withdrawal, while sg*Casp9* cells were protected from both STS and INS withdrawal (Figure 5E).

Initiation and nucleation steps of autophagosome biogenesis are not affected by CASP9 KO

Autophagosome biogenesis can be divided into phagophore initiation, nucleation, expansion, and closure of phagophore membranes, which generate the complete autophagosome [32]. Then, autophagosomes mature into autolysosomes through fusion with lysosomes for degradation and recycling of the cargos [32]. Each step is mediated by distinct ATG proteins and regulatory molecules. Since *CASP9* KO impaired autophagosome maturation into autolysosome, we examined

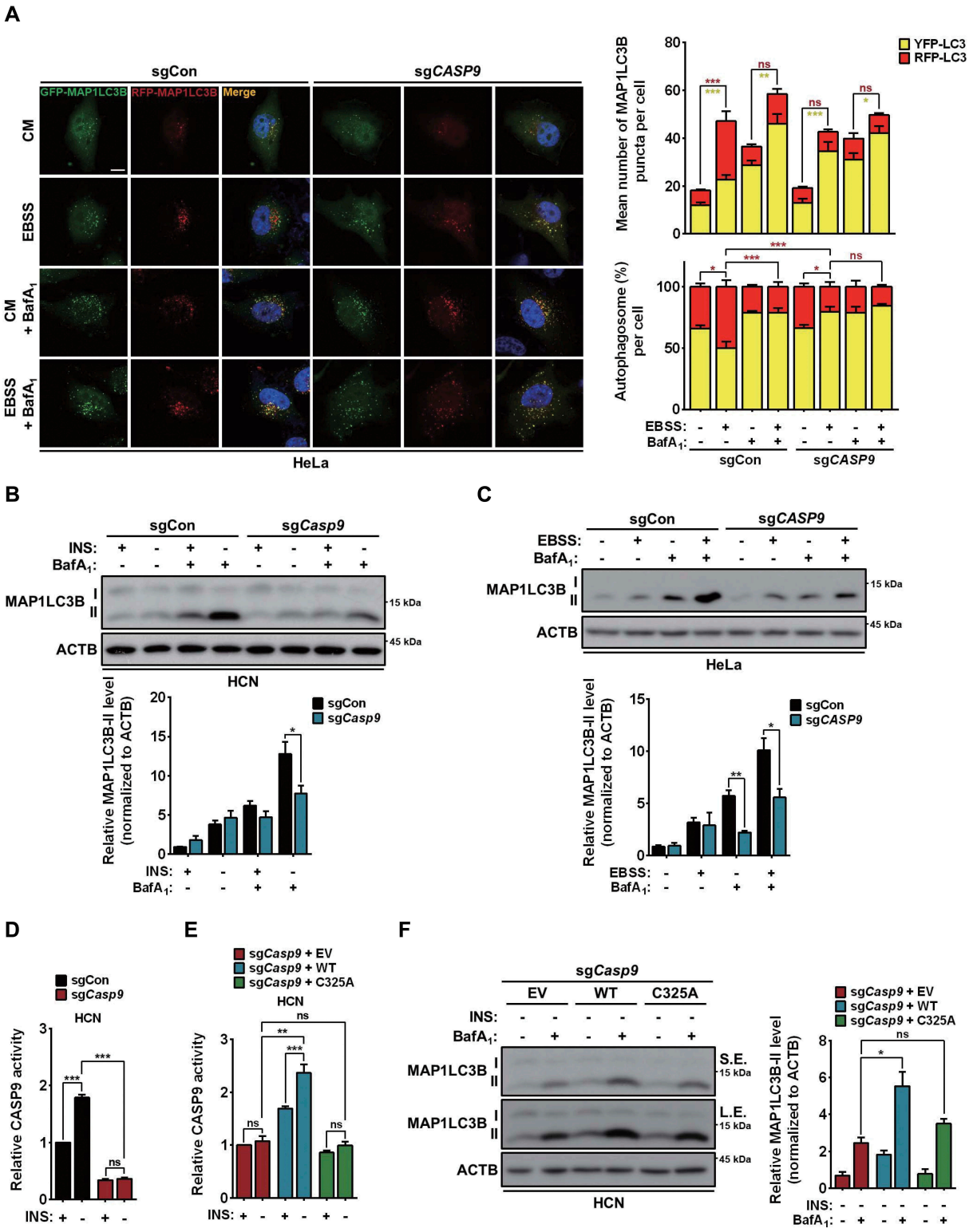

Figure 4. Genetic ablation of *CASP9* impairs autophagy flux. (A) Measurement of autophagy flux by mRFP-GFP-MAP1LC3B puncta assay after AA starvation for 1 h in sgCon and sg*CASP9* HeLa cells. $BafA_1$ (100 nM) was present during AA starvation. Graph, quantification of mRFP-GFP-MAP1LC3B puncta (n = 10 cells per condition). Scale bar: 10 μm. $^{*}P < 0.05$ and $^{***}P < 0.001$; ns, not significant for red MAP1LC3B puncta. $^{*}P < 0.05$, $^{**}P < 0.01$, and $^{***}P < 0.001$; ns, not significant for yellow MAP1LC3B puncta. (B) Western blotting analysis of MAP1LC3B after INS withdrawal for 6 h in sgCon and sg*Casp9* HCN cells. $BafA_1$ (10 nM) was added 1 h before cell harvest. Graph, quantification of MAP1LC3B-II normalized to ACTB (n = 4). (C) Western blotting analysis of MAP1LC3B after AA starvation for 1 h in sgCon and sg*CASP9* HeLa cells. $BafA_1$ (100 nM) was present during AA starvation. Graph, quantification of MAP1LC3B-II normalized to ACTB (n = 4). (D) CASP9 activity after INS withdrawal for 3 h in sgCon and sg*Casp9* HCN cells (n = 3). (E) CASP9 activity after INS withdrawal for 3 h in sg*Casp9* HCN cells transfected with EV, WT, or C325A *RnCasp9* (n = 4). (F) Western blotting analysis of MAP1LC3B after INS withdrawal for 6 h in sg*Casp9* HCN cells transfected with EV, WT, or C325A *RnCasp9*. $BafA_1$ (10 nM) was added 1 h before cell harvest (n = 3). S. E., short exposure; L. E., long exposure. $^{*}P < 0.05$, $^{**}P < 0.01$, and $^{***}P < 0.001$; ns, not significant.

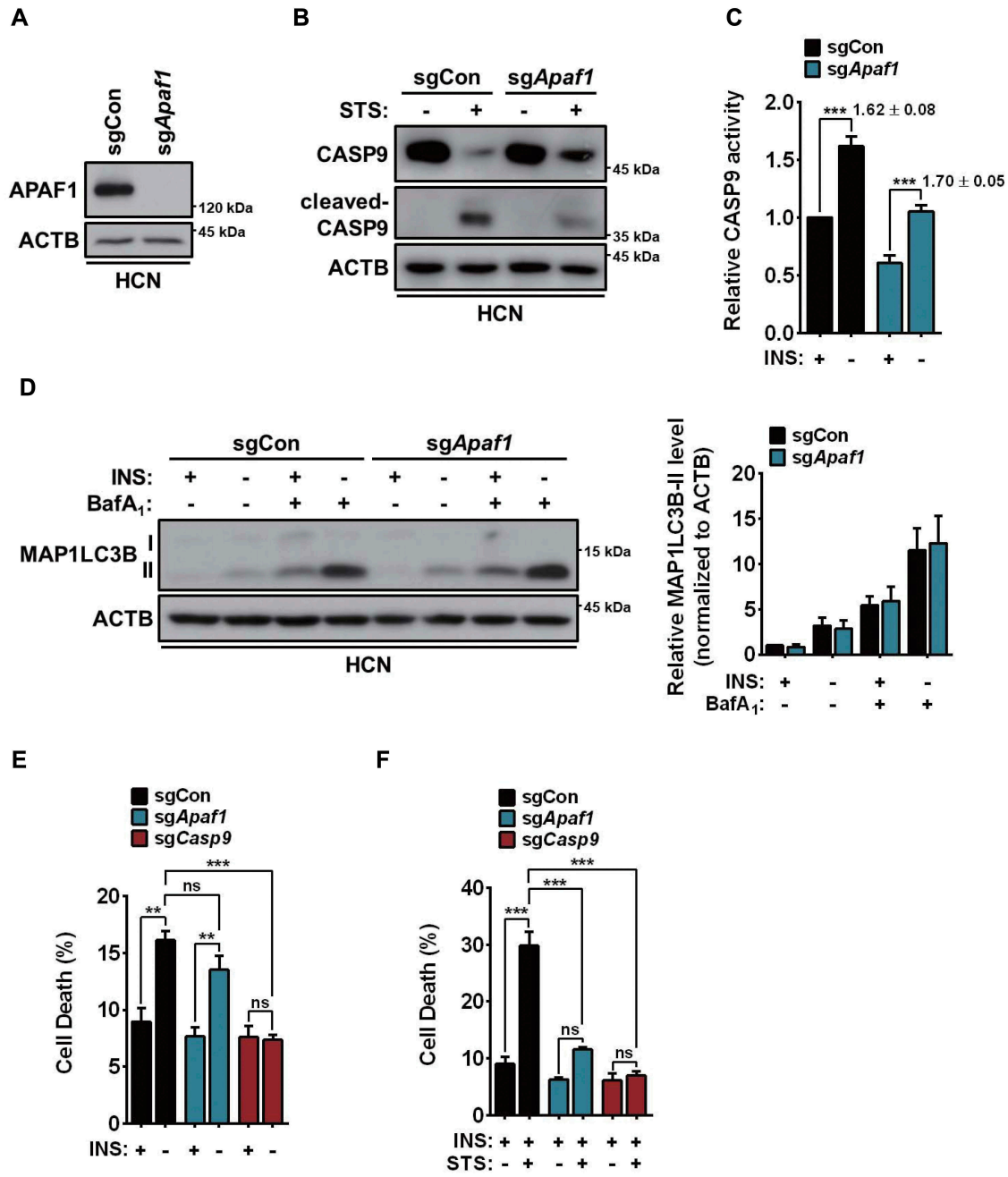

Figure 5. APAF1 is not required for CASP9 cleavage and autophagy induction following INS withdrawal in HCN cells. (A) Western blotting analysis for validation of *Apaf1* KO. (B) Western blotting analysis for evaluation of the effect of *Apaf1* KO on CASP9 cleavage after treatment with STS (0.5 μM, 6 h). The blots shown are representative of 3 experiments with similar results. (C) CASP9 activity after INS withdrawal for 3 h in sgCon and sg*Apaf1* cells (n = 4). (D) Western blotting analysis of MAP1LC3B after INS withdrawal for 6 h in sgCon and sg*Apaf1* cells. $BafA_1$ (10 nM) was added 1 h before cell harvest. Graph, quantification of MAP1LC3B-II normalized to ACTB (n = 3). (E) Cell death rate in sgCon, sg*Apaf1* and sg*Casp9* cells following INS withdrawal for 24 h (n = 4). (F) Cell death rate in sgCon, sg*Apaf1* and sg*Casp9* cells after treatment of STS for 12 h (n = 4). $^{**}P < 0.01$, $^{***}P < 0.001$; ns, not significant.

whether other autophagy steps are also affected. Autophagy initiation is induced by a kinase complex containing ULK1/Atg1 (unc-51 like autophagy activating kinase 1), which is under negative control by mechanistic target of rapamycin complex 1 (MTORC1) depending on nutrient status [33,34]. Therefore, we examined the phosphorylation status of autophagy upstream kinases MTOR at S2448 as an indicator of MTOR activity [35,36] and ULK1 at S757, which is a site for inhibitory phosphorylation by MTORC1 [33]. We also probed phosphorylation of BECN1 at S14 (rat numbering; S15 in humans), which is a substrate of ULK1 [34]. In both HCN and HeLa cells, phosphorylation of MTOR S2448 and ULK1 S757 was markedly reduced, while BECN1 phosphorylation was increased by INS withdrawal or AA starvation; the patterns of these changes were the same in *CASP9* KO and control cells (Figure 6A,B). These data indicate that upstream signaling molecules for autophagy initiation were not affected by *CASP9* KO.

Nucleation is mediated by a class III PtdIns3K complex composed of PIK3C3/Vps34, BECN1/Vps30/Atg6, PIK3R4/

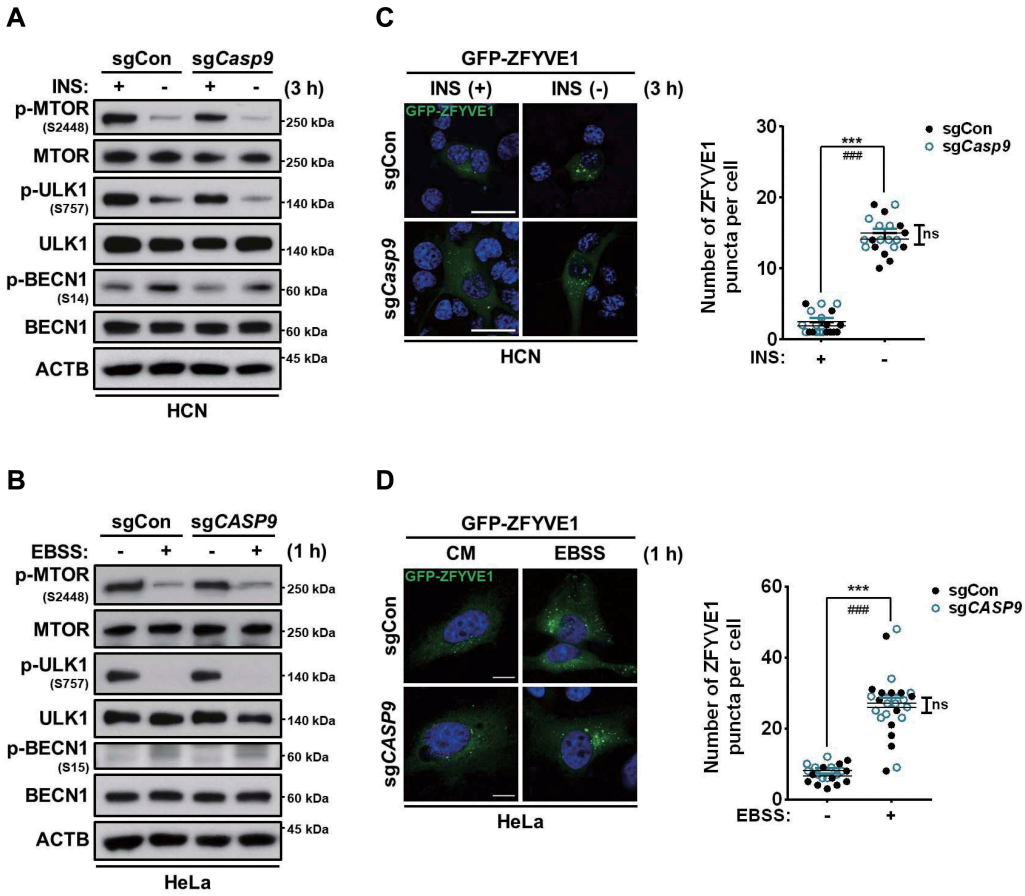

Figure 6. Initiation and nucleation steps of autophagosome formation are not affected by *CASP9* KO. (A and B) Western blotting analysis of phosphorylation of MTOR (S2448), ULK1 (S757), and BECN1 (S14, S15) after INS withdrawal (3 h) or AA starvation (1 h) in HCN (A) or HeLa (B) cells. The blots shown are representative of 3 experiments with similar results. (C and D) GFP-ZFYVE1 puncta assay after INS withdrawal (3 h) in HCN cells (C) or AA starvation (1 h) in HeLa cells (D). Graphs, quantification of the number of GFP-ZFYVE1 puncta (n = 10 cells per condition). Scale bar: 5 μm (HCN) and 10 μm (HeLa). $^{***}P < 0.001$ for sgCon cells. $^{###}P < 0.001$ for sg*Casp9* or sg*CASP9* cells. ns, not significant between control and *CASP9* KO cells after INS withdrawal or AA starvation.

Vps15, and ATG14 [37]. The increased phospholipid kinase activity produces PtdIns3P at the omegasome (a specialized ER subdomain for phagophore formation) and drives autophagosome formation by recruiting other ATG proteins and PtdIns3P effector proteins, such as ZFYVE1/DFCP1 (zinc finger FYVE-type containing 1) [38]. Therefore, the sites of phagophore nucleation and assembly can be examined by ZFYVE1. We assessed the number of GFP-ZFYVE1 puncta following autophagy induction and found that INS withdrawal or AA starvation induced the same number of ZFYVE1 puncta in *CASP9* KO and control cells, both HCN and HeLa (Figure 6C,D). These results demonstrate that the initiation and nucleation steps of autophagosome formation are intact in *CASP9* KO cells and CASP9 affects more downstream stages of autophagy, as suggested by the analysis of mRFP-GFP-MAP1LC3B puncta.

Autophagosome closure and maturation are impaired by CASP9 KO

Since autophagosome formation begins normally in *CASP9* KO cells, we checked whether ATG conjugation molecules are affected by *CASP9* KO. Western blotting analysis revealed that ATG3 was accumulated at high levels in *CASP9* KO HCN and HeLa cells (Figure 7A). Therefore, we checked whether transcription of *ATG3* was affected by *CASP9* KO. However, mRNA levels were not changed by *CASP9* KO in either HCN or HeLa cells (Figure 7B).

MAP1LC3B and other Atg8-family members undergo lipidation during autophagy induction and all of them are important for autophagosome formation, yet with different roles. MAP1LC3B is involved in elongation of the autophagosome membrane, whereas GABARAP members act at a later stage, in autophagosome maturation and closure [39]. Therefore, we examined the lipidated forms of GABARAP, GABARAPL1, and GABARAPL2 [39,40]. Interestingly, upon autophagy induction, increases in type II forms of GABARAPL1 and GABARAPL2 were markedly suppressed in *CASP9* KO cells, whereas no changes were observed in the lipidation of GABARAP (Figure 7C,D). These results showed that lipidation of GABARAPL1 and GABARAPL2 (Figure 7C,D) as well as MAP1LC3B (Figure 4B,C) was disturbed by *CASP9* KO. To reveal any differences in lipidation between MAP1LC3B and GABARAP members, western blotting analysis with a time-course after $BafA_1$ treatment was performed at basal state. This analysis showed that lipidation of GABARAPL2 in HCN cells and of GABARAPL1 and 2 in HeLa cells was significantly impaired in constitutive autophagy (Figure 7E,F). The reduced

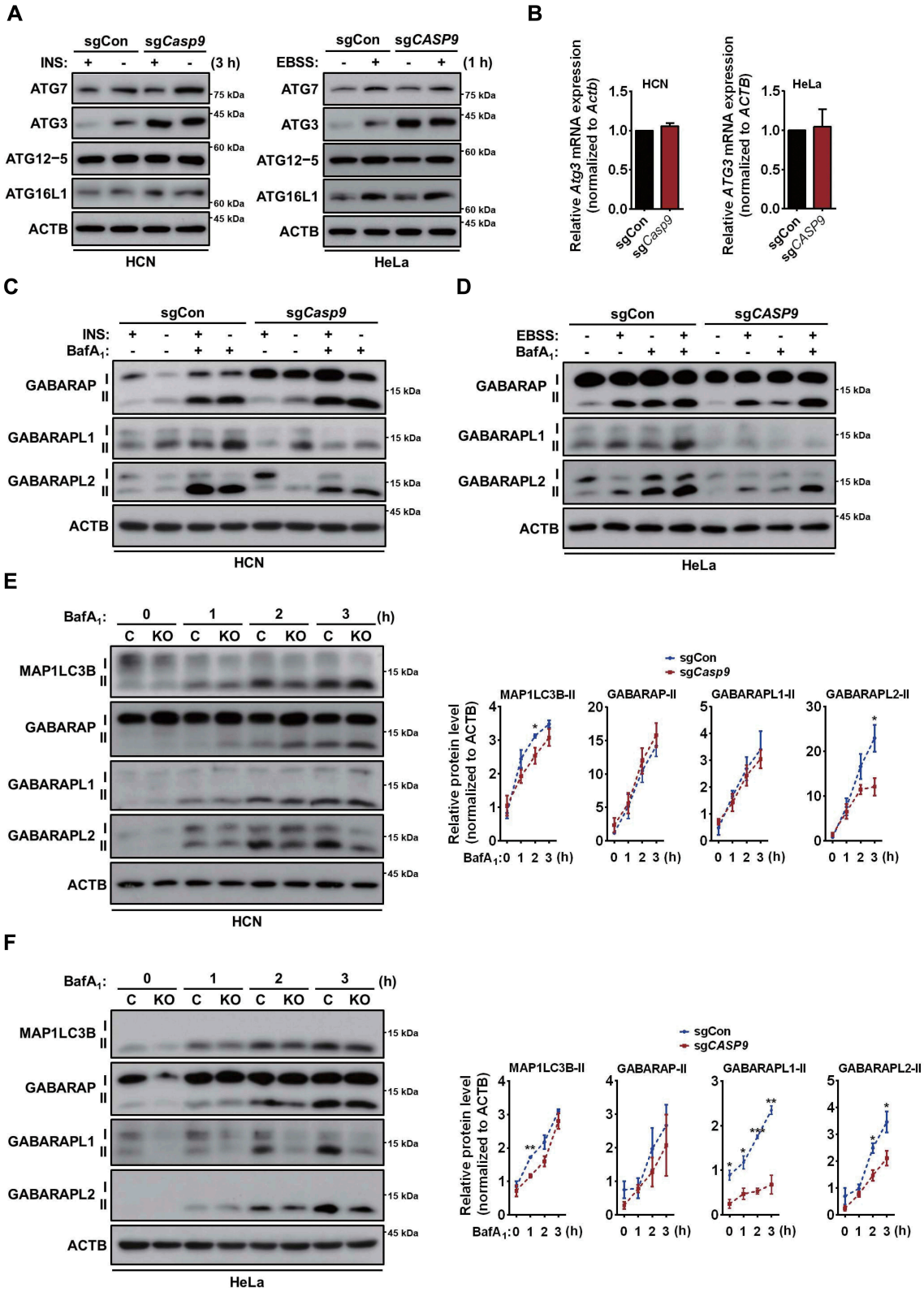

Figure 7. Lipidation of GABARAPL1 and GABARAPL2 is affected by *CASP9* KO. (A) Western blotting analysis of ATG-conjugating molecules, ATG7, ATG12–5, ATG16L1, and ATG3, after INS withdrawal (3 h) in HCN cells or AA starvation (1 h) in HeLa cells. The blots shown are representative of 3 experiments with similar results. (B) Relative mRNA levels of *Atg3*/*ATG3* in HCN or HeLa cells, respectively (n = 3). (C and D) Western blotting analysis of GABARAP family proteins after INS withdrawal (6 h) in HCN (C) cells or AA starvation (1 h) in HeLa cells (D). $BafA_1$ (10 nM for HCN cells; 100 nM for HeLa cells) was added 1 h before cell harvest in HCN cells or was present during AA starvation in HeLa cells. The blots shown are representative of 3 experiments with similar results. (E and F) Time-course analysis of lipidation of MAP1LC3B, GABARAP, GABARAPL1, and GABARAPL2 by western blotting in sgCon and sg*Casp9* HCN cells following treatment with $BafA_1$ (10 nM) (E) or in sgCon and sg*CASP9* HeLa cells following treatment with $BafA_1$ (100 nM) (F). Graphs, quantification of MAP1LC3B-II, GABARAP-II, GABARAPL1-II, and GABARAPL2-II normalized to ACTB (n = 3). *$P < 0.05$, **$P < 0.01$, and ***$P < 0.001$.

amounts of lipidated forms of MAP1LC3B and GABARAP members were not due to alternations in their transcript levels (data not shown). Given the potential involvement of GABARAP proteins in the late stages of autophagosome formation, these data support our observations that suppression of autophagy flux caused by *CASP9* KO is related to impaired autophagosome maturation.

A recent study using *atg3* KO mouse embryonic fibroblasts showed that, although phagophore formation was normal, the success rate of mature autophagosome formation was much lower and autophagosomes were deformed and had defective degradation of the IAM [40]. In this study, GFP-tagged STX17 (syntaxin 17) was used as a marker of autophagosome maturation, since elongating phagophore membrane is STX17-negative until it becomes completely ring-shaped. STX17 is then recruited and eventually released after autophagosome–lysosome fusion and IAM degradation [40]. Therefore, we adopted the GFP-STX17 construct to monitor autophagosome membrane closure and maturation. We first counted the number of ring-shaped STX17-positive structures, which correspond to closed autophagosomes. In sgCon HeLa cells, the number of such structures increased significantly at an early time point (0.5 h) and then gradually decreased (Figure 8A). In sg*CASP9* cells, their number was significantly lower than in sgCon cells and no significant increase at 0.5 h was observed (Figure 8A). We also noticed an irregular shape of STX17-positive autophagosomes in sg*CASP9* cells (Figure 8A). To analyze the shape of STX17-positve structures at higher resolution, we used super-resolution structured illumination microscopy (SR-SIM). In control cells, fully closed, circular STX17-containing autophagosome were detected following autophagy induction. However, in *CASP9* KO cells, STX17-positive autophagosomes were not closed and had a distorted shape (Figure 8B). Next, we measured the lifetime of STX17-containing autophagosomes during starvation by live confocal imaging of GFP-STX17 in living cells. In control cells, most of the STX17 rings disappeared within 20 min (average lifetime, 13.55 ± 0.82 min), suggesting that it takes less than 20 min for fusion with lysosomes and degradation of the IAM. In contrast, the lifetime of STX17 rings in sg*CASP9* cells was 30.90 ± 3.24 min, more than twice as long as that in sgCon cells (Figure 8C). These results clearly indicate that autophagosome maturation, including sealing of the membranes, fusion with lysosomes, and subsequent degradation of the IAM, was significantly delayed by *CASP9* KO. Autophagosomes are matured and degraded by fusion with late endosomes [41,42]. Since autophagosome degradation was delayed in *CASP9* KO, fusion with late endosomes is likely also suppressed in *CASP9* KO cells. RAB7 is a well-characterized marker of late endosomes [41]; therefore, we checked co-localization of MAP1LC3B and SQSTM1 with RAB7. As expected, RAB7 was strongly co-localized with MAP1LC3B or SQSTM1 after AA starvation in sgCon HeLa cells. However, this co-localization was considerably decreased by *CASP9* KO (Figure 8D,E).

Lastly, we confirmed the deformed morphology of autophagosomes by transmission electron microscopy in HeLa cells. We first checked the state of autophagosome closure in sgCon and sg*CASP9* at basal state. Closed or unclosed autophagosomes were detected in both sgCon and sg*CASP9* cells, and the number of closed autophagosomes was similar between sgCon and sg*CASP9* cells at basal state (Figure 8F,G). However, the number of unclosed autophagosomes was significantly higher in *CASP9* KO cells, indicating inefficient autophagosome closure. These results strongly suggest that CASP9 activity is required for autophagosome closure and maturation.

Production of mitochondrial ROS is decreased in CASP9 KO cells

One of the mechanisms modulating autophagy acts through ROS-mediated pathways [43]. Endogenous ROS formation can have disparate effects on autophagy. ROS, especially mitochondrial superoxide is critical for stimulation of autophagy [44–46]. However, overtly elevated level of intracellular ROS may compromise autophagy by oxidative inhibition of ATG3 and ATG7 [47]. Since the effects of *CASP9* KO on ATG3 seemed to be at the protein level, we wondered if the production of mitochondrial ROS is altered in *CASP9* KO cells. To detect generation of mitochondrial superoxide, we used MitoSOX Red. Of note, basal level of mitochondrial ROS was markedly reduced, and generation of mitochondrial ROS induced by AA starvation was also greatly diminished in sg*CASP9* HeLa cells (Figure 9A,B). When measured using another ROS indicator, chloromethyl-2′,7′-dichlorodihydrofluorescein diacetate (CM-H_2 DCFDA), the intracellular ROS level was also significantly lower in sg*CASP9* cells than in sgCon cells (Figure 9C). These data suggest that *CASP9* KO decreased production of endogenous ROS below the level required to stimulate autophagy. Thus, we reasoned that addition of extracellular ROS in the form of H_2O_2 could rescue autophagy flux. Frudd et al. reported that a high concentration of extracellular H_2O_2 (over 200 μM) inhibits autophagy by oxidation of ATG3 and ATG7 [47]. Therefore, we treated sg*CASP9* HeLa cells with low doses of H_2O_2 and examined whether lipidation of MAP1LC3B and GABARAPL2 would be restored. As we anticipated, doses of H_2O_2 below 50 μM rescued autophagy flux within 1 h after addition to AA-starved sg*CASP9* HeLa cells (Figure 9D). These data suggest that curtailed level of endogenous ROS, including mitochondrial superoxide, underlies the inefficient conjugation of MAP1LC3B and GABARAPL2.

To determine if ATG3 activity was inhibited in the absence of CASP9, we compared the endogenous levels of the ATG3-Atg8-family protein (referred to here as ATG8 for the mammalian homologs of yeast Atg8) intermediates in sgCon and sg*CASP9* cells with sg*ATG3* cells as a negative control for ATG3 and ATG3-ATG8 bands. We performed non-reducing western blotting analysis following the published procedure [47] and observed significant decrease in the amounts of ATG3-ATG8 intermediates in sg*CASP9* cells after AA starvation (Figure 9E). To further confirm inhibition of ATG3 activity in *CASP9* KO cells, we generated *ATG3* and *CASP9* double KO HeLa cells (sg*ATG3;CASP9*) and expressed FLAG-tagged

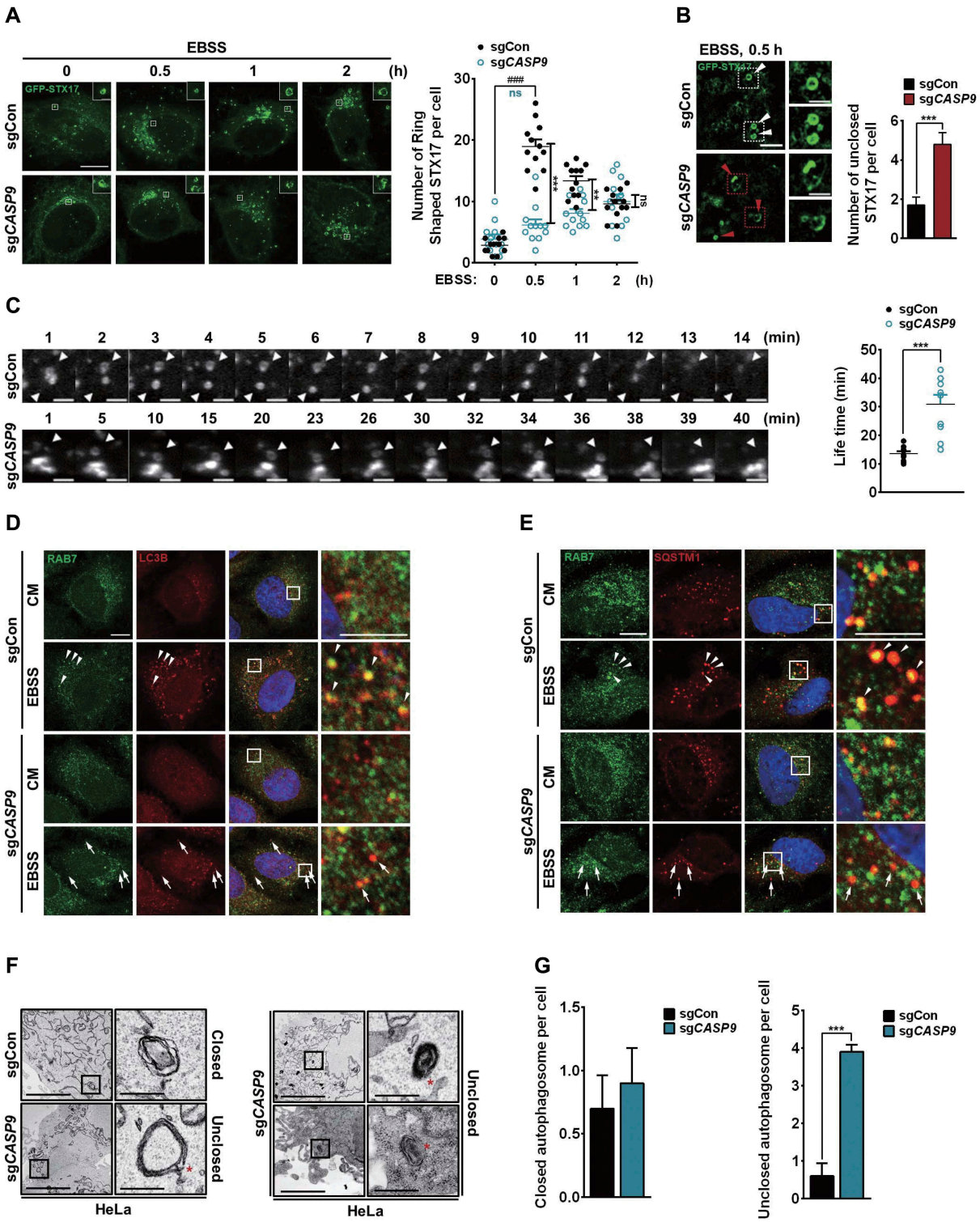

Figure 8. Autophagosome closure is impaired by *CASP9* KO. (A) Expression of GFP-STX17 in sgCon and sg*CASP9* HeLa cells. Ring-shaped STX17 structures were analyzed following AA starvation at the indicated time points. Graph, number of GFP-STX17 puncta per cell (n = 10 cells at each time point). Scale bar: 10 μm. $^{**}P < 0.001$ and $^{***}P < 0.001$; ns, not significant between sgCon and sg*CASP9* cells. $^{###}P < 0.001$ compared to the control (0 h) in sgCon cells. ns, not significant compared to the control (0 h) in sg*CASP9* cells. (B) High-resolution images of STX17-positive structures captured by super-resolution structured illumination microscopy (SR-SIM) in sgCon and sg*CASP9* HeLa cells after AA starvation for 0.5 h. White and red arrowheads indicate complete and unclosed STX17 structures, respectively. Scale bar: 5 μm (2 μm for magnified images). Graph, number of GFP-STX17 puncta per cell (n = 10 cells). (C) Measurement of lifetime of GFP-STX17-containing autophagosomes by live-imaging confocal microscopy following AA starvation. Arrowheads indicate STX17-positive rings (n = 10 in at least 8 cells). Scale bar: 2 μm. (D) Co-localization of endogenous RAB7 and MAP1LC3B in sgCon and sg*CASP9* HeLa cells after AA starvation for 2 h. Scale bar: 10 μm (5 μm for magnified images). (E) Co-localization of endogenous RAB7 and SQSTM1 in sgCon and sg*CASP9* HeLa cells after AA starvation for 2 h. Arrowheads indicate co-localization and arrows indicate MAP1LC3B or SQSTM1 without RAB7. Scale bar: 10 μm (5 μm for magnified images). (F) Analysis of autophagosome morphology by transmission electron microscopy in sgCon and sg*CASP9* HeLa cells. Red asterisks indicate the region of unclosed at autophagosome. Scale bar: 5 μm (500 nm for magnified images). (G) Quantification of closed and unclosed autophagosomes in sgCon and sg*CASP9* cells (n = 10). $^{***}P < 0.001$.

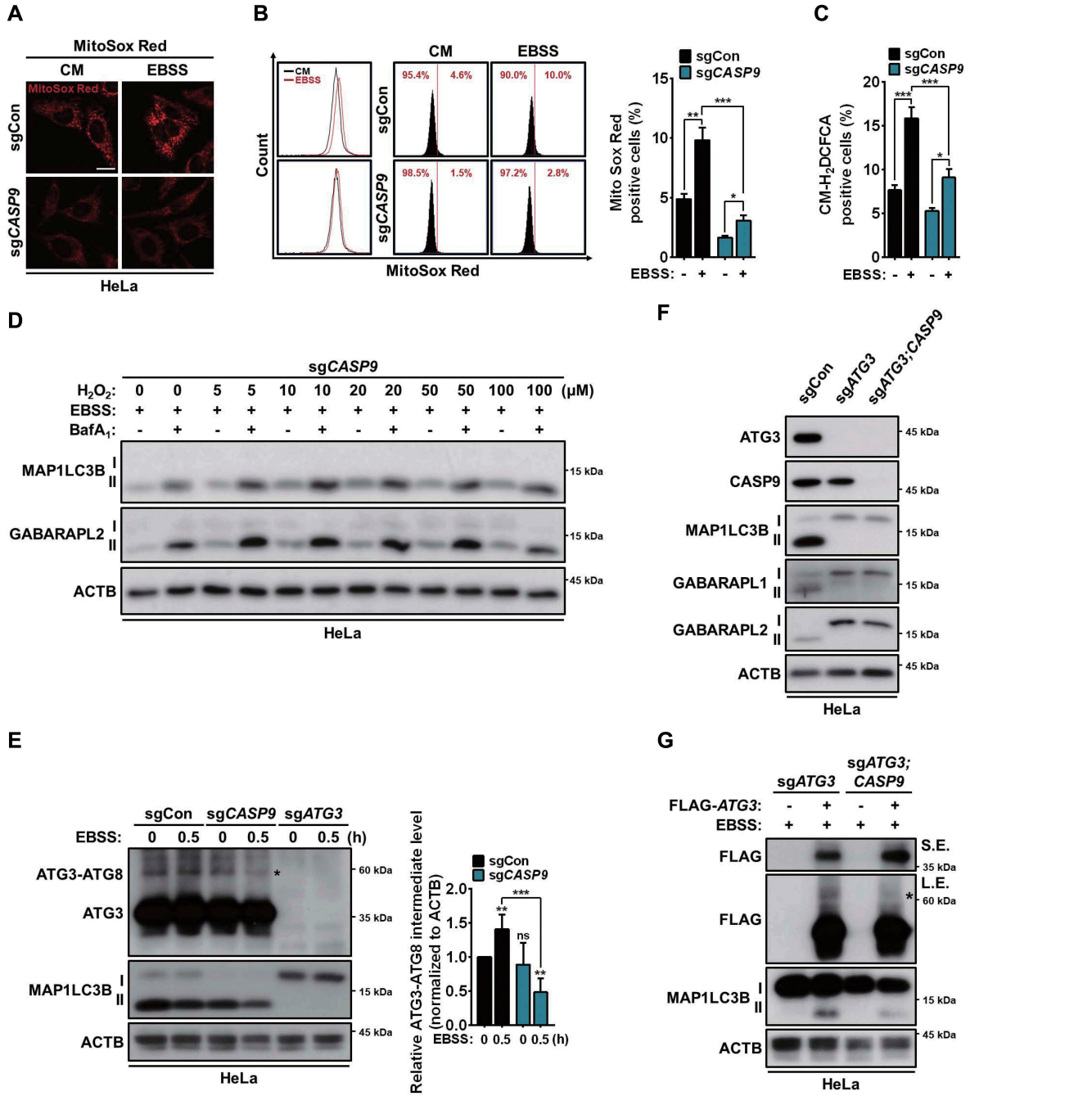

Figure 9. Production of mitochondrial ROS is suppressed by *CASP9* KO. (A) Analysis of mitochondrial ROS production. sgCon and sg*CASP9* HeLa cells were stained with MitoSox Red (5 μM) for 30 min following AA starvation (15 min) and analyzed using live-imaging confocal microscopy. Scale bar: 20 μm. (B) Measurement of mitochondrial ROS production by fluorescence-activated cell sorting (FACS). sgCon and sg*CASP9* HeLa cells after AA starvation for 1 h were stained with MitoSox Red (5 μM) for 15 min. (C) Measurement of intracellular ROS by FACS. sgCon and sg*CASP9* HeLa cells after AA starvation for 1 h were stained with CM-H_2DCFDA (200 nM) for 20 min. (D) Western blotting analysis of MAP1LC3B and GABARAPL2 lipidation after AA starvation for 1 h in HeLa cells. H_2O_2 was added 1 h before medium change to EBSS. (E) Non-reducing western blotting analysis of ATG3-ATG8 intermediate after AA starvation for 0.5 h in sgCon, sg*CASP9* and sg*ATG3* HeLa cells, respectively. sg*ATG3* cells were used as a negative control of ATG3 and ATG3-ATG8 intermediate bands. Asterisk indicates ATG3-ATG8 intermediate band. Graph, quantification of ATG3-ATG8 intermediates normalized to ACTB (n = 3). (F) Western blotting analysis of ATG3, CASP9 and Atg8-family lipidation in sgCon, sg*ATG3* and sg*ATG3;CASP9* HeLa cells. (G) Non-reducing western blotting analysis of FLAG-ATG3-ATG8 intermediate after AA starvation for 0.5 h in sg*ATG3* and sg*ATG3;CASP9* cells without or with expressing FLAG-ATG3. Asterisk indicates FLAG-ATG3-ATG8 intermediate band. The blots shown are representative of 3 experiments with similar results. *$P < 0.05$, **$P < 0.01$, ***$P < 0.001$.

WT ATG3 in sg*ATG3* or sg*ATG3;CASP9* cells. Lipidation of Atg8-family proteins was completely blocked in sg*ATG3* and sg*ATG3;CASP9* cells (Figure 9E,F) and expression of ATG3 restored the level of MAP1LC3B lipidation in sg*ATG3*, but not in sg*ATG3;CASP9* cells (Figure 9G). The amount of FLAG-ATG3-ATG8 intermediate was also much less in sg*ATG3;*

CASP9 cells than sg*ATG3* cells (Figure 9G). These data indicate that ATG3 activity was inhibited in *CASP9* KO cells.

Mitochondrial homeostasis is disrupted by CASP9 KO

A marked decline in mitochondrial ROS production, even under starvation, in *CASP9* KO cells implies dysregulated mitochondrial function. Therefore, we compared the mitochondrial membrane potential (Δψm) in sgCon and sg*CASP9* HeLa cells by staining with tetramethylrhodamine ethyl ester (TMRE) and found that basal Δψm was lower in sg*CASP9* cells (Figure 10A). Next, we used MitoTracker Green to assess the total number of mitochondria and MitoTracker Deep Red to measure mitochondrial membrane potential. In agreement with TMRE data, we observed an increase in the population of depolarized mitochondria in sg*CASP9* cells (Figure 10B). Since the morphological dynamics of mitochondria is associated with their key physiological functions, including cell death, bioenergetics, and autophagy [48], we monitored mitochondrial morphology in living cells stained with MitoTracker Green by live confocal

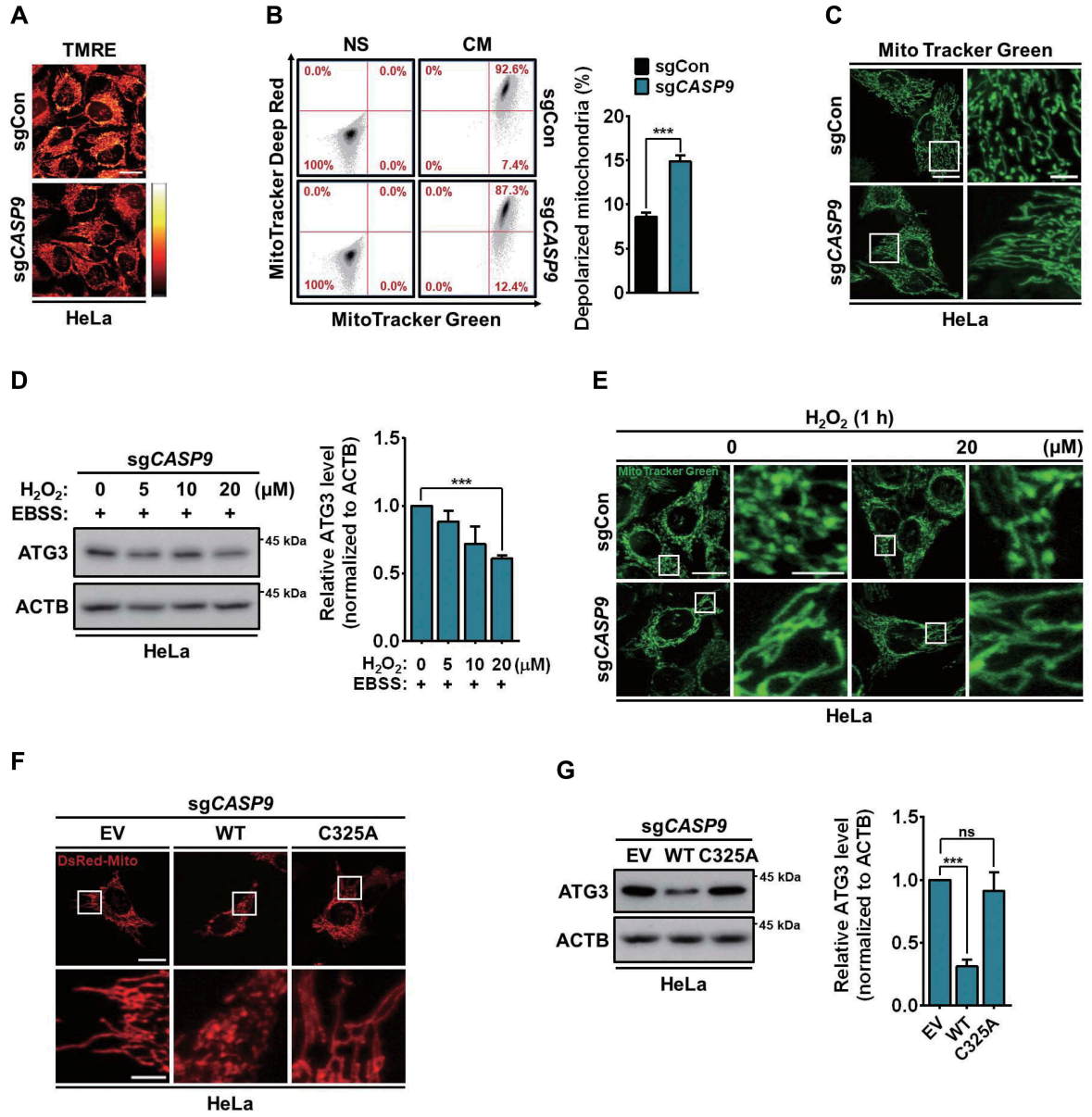

Figure 10. Mitochondrial morphology and homeostasis are affected by *CASP9* KO. (A) Measurement of mitochondrial membrane potential (Δψm). sgCon and sg*CASP9* HeLa cells were stained with TMRE (100 nM, 20 min) and analyzed using live-imaging confocal microscopy. Scale bar: 20 μm. (B) Analysis of depolarized mitochondria by FACS. sgCon and sg*CASP9* HeLa cells were stained with MitoTracker Green and MitoTracker Deep Red (100 nM each, 20 min; n = 4). (C) Mitochondrial morphology. sgCon and sg*CASP9* HeLa cells were stained with MitoTracker Green (200 nM, 20 min) and analyzed using live-imaging confocal microscopy. Scale bar: 20 μm (5 μm for magnified images). (D) Western blotting analysis of ATG3 protein level after AA starvation for 1 h in sg*CASP9* HeLa cells. H_2O_2 was added 1 h before medium change to EBSS. Graphs, quantification of ATG3 normalized to ACTB (n = 3). (E) Mitochondrial morphology. sg*CASP9* HeLa cells were treated with H_2O_2 (20 μM, 1 h), stained with MitoTracker Green (200 nM, 20 min), and analyzed using live-imaging confocal microscopy. Scale bar: 20 μm (5 μm for magnified images). (F) Mitochondrial morphology. sg*CASP9* HeLa cells co-transfected with DsRed-Mito and EV, WT, or C325A *RnCasp9* (1:3 ratio) were analyzed using live-imaging confocal microscopy. Scale bar: 20 μm (5 μm for magnified images). (G) Western blotting analysis of ATG3 protein level after introduction of EV, WT, or C325A *RnCasp9* into sg*CASP9* HeLa cells. Graphs, quantification of ATG3 normalized to ACTB (n = 3). ***$P < 0.001$; ns, not significant.

microscopy. Interestingly, *CASP9* deletion resulted in a transition from the tubular or globular shape of normal mitochondria with diverse lengths to an entangled, long tubular shape (Figure 10C). To further examine the differences in mitochondrial dynamics between control and *CASP9* KO cells, we transfected cells with DsRed-Mito and performed real-time tracking of mitochondria. In sgCon HeLa cells, mitochondria actively moved and constantly connected with and disconnected from other mitochondria (Movie S1). However, mitochondria remained interconnected and formed long tubular structure in sg*CASP9* cells, and mitochondrial fusion and fission occurred at a much lower rate than in sgCon cells (Movie S2). These results indicate that CASP9 is critical for mitochondrial fusion and fission and maintenance of their normal morphology. Since extracellularly added H_2O_2 rescued autophagy flux, we checked whether mitochondrial defects were also corrected. Interestingly, H_2O_2 addition rescued the abnormal accumulation of ATG3 (Figure 10D) but not dysregulated mitochondrial morphology (Figure 10E). Conversely, expression of active CASP9 corrected both the ATG3 levels and mitochondrial morphology, indicating that mitochondrial phenotypes are caused by loss of CASP9 (Figure 10F,G and Movies S3-5).

Next, we checked whether the proteins regulating mitochondrial fusion and fission were affected by *CASP9* KO. Interestingly, DNM1L/DRP1 (dynamin 1 like), MFN1 (mitofusin 1) and MFN2 were significantly accumulated in sg*CASP9* cells (Figure 11A). Furthermore, inactive form of DNM1L, as indicated by S637 phosphorylation was increased while active form of DNM1L, as indicated by S616 phosphorylation was decreased in sg*CASP9* cells, indicating defects in DNM1L function and mitochondria fission in sg*CASP9* cells (Figure 11A). To examine whether inhibition of mitochondria fission was able to recapitulate autophagy defects observed in CASP9-deficient cells, we expressed dominant-negative (DN) form of DNM1L and monitored mitochondria morphology and lipidation of ATG8 proteins. In a similar way to sg*CASP9* cells, expression of DN-DNM1L showed long and hyperconnected mitochondria morphology (Figure 11B) with reduced lipidation of ATG8 proteins (Figure 11C). These data suggest that CASP9 can affect the stability and function of protein regulating mitochondrial fission and fusion. To examine whether CASP9 translocate to mitochondria upon autophagy induction, we performed subcellular fraction into mitochondrial and cytosolic fractions with starved HeLa cells. Interestingly, we observed pro and cleaved forms of CASP9 in the mitochondrial fraction at both basal and starved states, whereas cytosolic fraction contained only proform of CASP9 at basal state and cleaved CASP9 was detected in the cytosol only after EBSS starvation (Figure 11D). Next, we wondered whether CASP9 activation was dependent on mitochondrial ROS. Activation of CASP9 in starved HeLa cells was significantly suppressed by Mito-TEMPO (Figure 11E,F). Combined with mitochondrial fractionation experiments, these results suggest that mitochondrial fraction of CASP9 is activated by mitochondrial ROS upon autophagy induction and amplifies signal for facilitation of autophagy. Although this speculation needs more experimental verification, it provides a useful starting point for further analysis. All together, these results clearly indicate that CASP9 activity is essential for mitochondrial homeostasis and optimal level of ROS generation, which are in turn required for membrane closure and completion of autophagosome formation in response to growth factor or nutrient deprivation.

Discussion

Physiological outcomes of crosstalk between autophagy and apoptosis, and related molecular mechanisms are quite complex. Generally, autophagy is considered a pro-survival mechanism to prevent cell death under stress conditions, while excessive level of stress leads cells to the point of no return, and apoptosis inhibits autophagy to promote cell death. Accordingly, accumulating evidence shows that CASPs suppress autophagy to facilitate apoptosis. However, CASPs have also been found to promote autophagy independently of their apoptotic function, or even in opposition to apoptosis [14,15]. Therefore, the function of CASPs in regulation of autophagy is not as simple as it might seem at first glance, and is rather context-dependent. The contradictory roles of CASPs in autophagy and relevant molecular mechanisms warrant further detailed investigation. In this study, we observed CASP9 activation during autophagy induction. However, CASP9 activation was autophagy-independent, because *Ulk1* KO or *Atg7* knockdown in HCN cells did not affect CASP9 activation. Although an increase in CASP9 activity was reduced in sg*Ulk1* or sh*Atg7* HCN cells following INS withdrawal, there was still significant upregulation of CASP9 activity (sgCon vs. sg*Ulk1* vs. sh*Atg7*; 1.72 ± 0.12 vs. 1.47 ± 0.02 vs. 1.45 ± 0.04, n = 3). CASP9 activation mediates ACD in INS-deprived HCN cells or does not evoke immediate cell death in AA-starved HeLa cells. Although CASP9 began to be activated from very early time points in HeLa cells (within 30 min by EBSS, as shown in Figure 1H), this early activation of CASP9 did not cause cell death (control vs. EBSS at 12 h; 1.49 ± 0.14% vs. 5.22 ± 0.38%, n = 3). As a control of cell death assay, 0.25 μM of STS caused a marked increase in cell death (61.24 ± 3.60% at 12 h, n = 3). This concentration of STS was used typically in HeLa cells [49]. In either way, CASP9 activation is associated with autophagy, not apoptosis. If CASP9 activity is indispensable for autophagy flux, then how does CASP9 activity not propagate apoptotic signal at the same time? And what can be its substrates/targets and underlying mechanisms for its role in autophagy regulation?

Although a few studies have already suggested a positive role of CASP9 in autophagy regulation, our study suggests previously unidentified molecular mechanisms. Han et al. reported that CASP9 forms a complex with ATG7 [14]; however, we were not able to observe this interaction under our experimental conditions. Also, in this reported direct interaction, CASP9 activity is not required for autophagy facilitation, and ATG7 suppresses CASP9 processing and its apoptotic activity. In contrast, our pharmacological and genetic inactivation studies demonstrate that CASP9 activity is critical for autophagy induction. Lending further support to our conclusion, rescue experiments showed that only WT CASP9, but not its inactive mutant, restored autophagy flux in *CASP9* KO cells. In breast cancer MCF-7 cells, CASP9 has a pro-survival function and protects against nonsteroidal anti-inflammatory drugs used as anticancer therapy by enhancing autophagy [15]. However, the

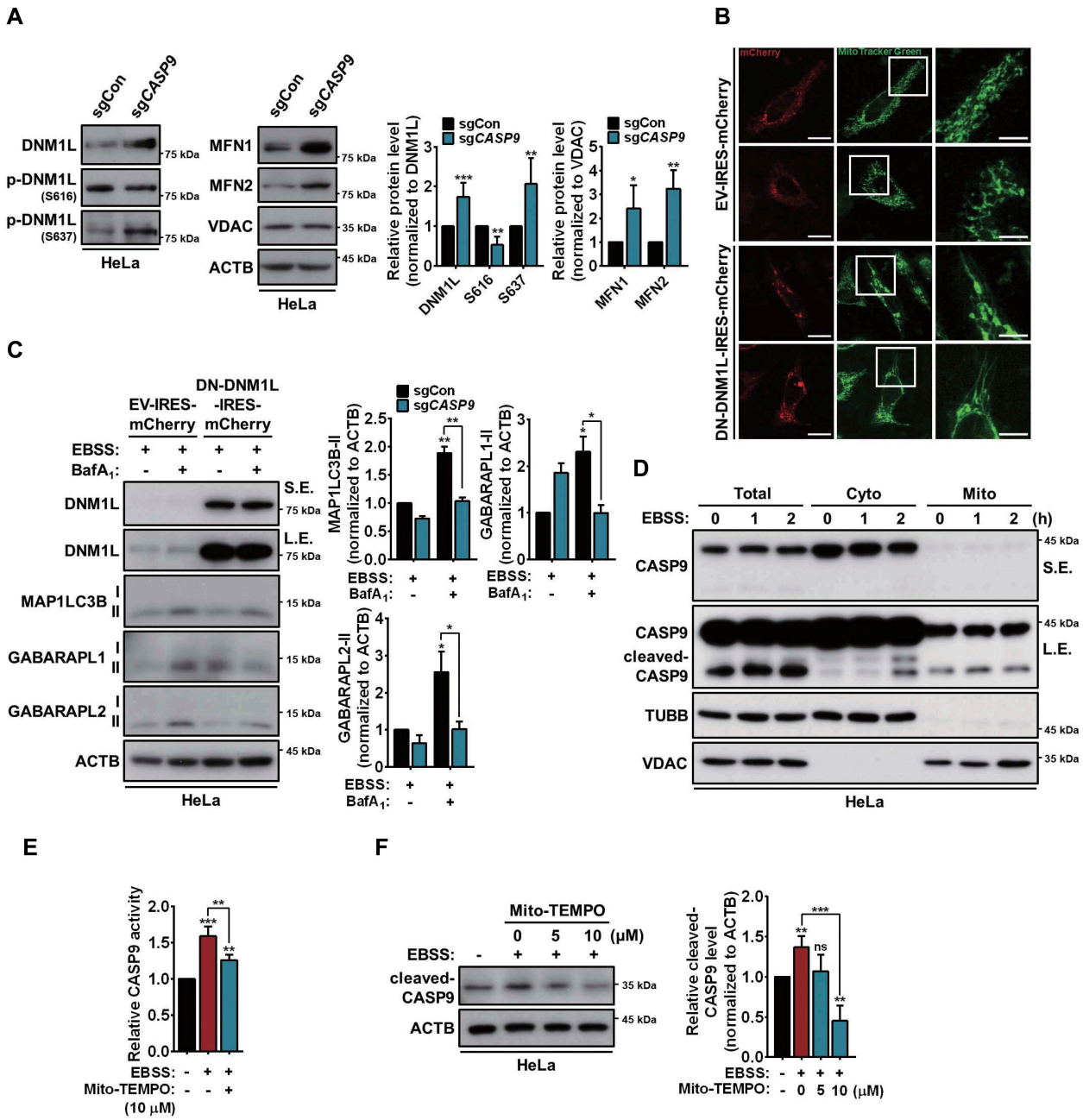

Figure 11. Mitochondrial fusion-fission proteins are affected by *CASP9* KO. (A) Western blotting analysis of mitochondrial fusion and fission proteins in sgCon and sg*CASP9* cells. Graphs, quantification of DNM1L, MFN1 and MFN2 normalized to ACTB or p-DNM1L S616 and S637 normalized to total DNM1L (n = 4). (B) Mitochondrial morphology after expression of DN-DNM1L. HeLa cells transfected with IRES-mCherry (EV) or DN-DNM1L-IRES-mCherry (DN-DNM1L) were stained with MitoTracker Green (200 nM, 20 min), and analyzed using live-imaging confocal microscopy. Scale bar: 20 μm (5 μm for magnified images). (C) Western blotting analysis of GABARAP1L, L2 and MAP1LC3B lipidation transfected with IRES-mCherry (EV) or DN-DNM1L-IRES-mCherry (DN-DNM1L) after AA starvation for 1 h without or with $BafA_1$ (100 nM) in HeLa cells (n = 3). (D) Western blotting analysis of mitochondrial localization of cleaved CASP9 in HeLa cells after AA starvation for the indicated time periods. Cyto and Mito represent cytoplasmic and mitochondria fractions, respectively. TUBB and VDAC were used as loading control of each fraction. (E) CASP9 activity in HeLa cells after AA starvation without or with Mito-TEMPO (10 μM) (n = 5). (F) Western blotting analysis of cleaved CASP9 after AA starvation for 1 h with Mito-TEMPO at the indicated concentrations (n = 4). Mito-TEMPO was added 2 h before medium change to EBSS. S. E., short exposure; L. E., long exposure. $^{*}P < 0.05$, $^{**}P$, $^{\#\#}P < 0.01$, $^{***}P < 0.001$; ns, not significant.

molecular mechanism for CASP9-mediated autophagy has not been resolved in that study. Our study suggests that CASP9 is likely to mediate autophagy induction through the mitochondrial pathway, especially through production of mitochondrial ROS. Mitochondrial ROS are implicated in autophagy induction under various conditions, including starvation and inhibition of the mitochondrial electron transport chain [44,46]. Our study, in line with the stimulatory role of ROS in autophagy, suggests that optimal production of mitochondrial ROS contributes to the progress of autophagy. However, the ROS-mediated redox events related to autophagosome elongation need to be further elucidated at the molecular level. The probable molecular target of ROS is ATG3 or ATG4. We observed a significant accumulation of ATG3 in *CASP9* KO cells. Although the molecular properties of the abnormally accumulated ATG3 in *CASP9* KO cells await further characterization, accumulated ATG3 is likely

to be inactive. Accumulation of ATG3 seems to be regulated posttranslationally, because its transcript level is not changed. We have excluded the possibility that ATG3 level is regulated through CASP9-dependent cleavage, because we could not detect any evidence of ATG3 cleavage by or its interaction with CASP9 (data not shown). Also, extracellular H_2O_2 quickly (within 1 h) reduces the ATG3 protein level to baseline in *CASP9* KO cells.

Lipidation status of MAP1LC3B/GABARAP members is regulated by reversible lipid conjugation [50]. ATG4 is a cysteine protease that processes ATG8 members in both conjugation and deconjugation steps. ATG4 cleaves nascent ATG8 proteins and exposes their C-terminal glycine residue. This cleavage is known as priming of MAP1LC3/GABARAP proteins and generates cytosolic MAP1LC3-I/GABARAP-I forms for PE conjugation. ATG4 also delipidates PE-conjugated MAP1LC3-II/GABARAP-II by breaking the bond between the C-terminal glycine and PE [51]. During starvation, ATG4 activity is inhibited by ROS through oxidation of the catalytically critical cysteine residue [44]. Therefore, in *CASP9* KO cells, which produce mitochondrial ROS at a much lower rate than control cells, ROS-mediated modulation of ATG4 activity is likely to be incomplete and ATG4 is expected to stay overactive despite autophagy induction. ATG4 then very rapidly releases PE from ATG8 proteins, especially GABARAPL1 and GABARAPL2. Since lipidated ATG8 proteins are involved in all aspects of autophagosome development, the diminished amount of lipidated MAP1LC3/GABARAP will considerably slow down autophagosome formation. Again, restoration of intracellular redox balance, by reconstitution with active CASP9 or addition of extracellular H_2O_2 to *CASP9* KO cells, rescues defective lipidation of MAP1LC3B or GABARAPL2. The priming of ATG8 proteins is fast and constitutive, and the resting level of ATG4 is enough to support priming [50]. On the other hand, sustained autophagosome growth requires persistent presence of MAP1LC3–PE/GABARAP–PE proteins. As such, delipidation of ATG8 members is not thought to be constitutive, nor as fast as priming [50]. Therefore, overactivation of ATG4 would more greatly affect delipidation than PE conjugation.

Another aspect to be investigated in the future is how CASP9 is activated. Since APAF1 is dispensable for CASP9 activation in HCN cells, there may be a distinct activation mechanism different from typical apoptotic pathways. One candidate mechanism is through autophagosome-mediated processing of CASP9, as hinted by the case of CASP8. CASP8 activation was reported in the absence of its conventional, death ligand receptor-dependent activation pathway [52]. Interestingly, CASP8 maturation following apoptosis induction is strongly impaired when autophagy is inhibited. Therefore, CASP8 is activated in an autophagosome-dependent way [16,53]. CASP9 may be activated in a similar manner. However, it should be mentioned that CAPS8 executes apoptosis after autophagosome-dependent activation, which is in contrast to association of CASP9 activation with autophagy in our study.

It would also be interesting to determine how CASP9 regulates mitochondrial homeostasis. Depolarization of mitochondrial outer membrane potential and subsequent CASP9 activation are well established in mitochondria-mediated intrinsic apoptosis [54]. CASP9 then induces feedback disruption of mitochondria [55]. However, in contrast to CASP-dependent mitochondrial damage during apoptosis, CASP9 activity is essential to maintain mitochondrial homeostasis at basal state and during autophagy induction under our experimental conditions. How the CASP9 signaling cascade is diverted from activation of downstream CASPs and apoptosis, and is instead driven toward autophagy needs further investigation. Also, little is known about how CASPs affect mitochondria in the nonapoptotic context. Given CASP9 activation without mitochondrial disruption and immediate apoptosis, our study will provide a useful platform for future study to understand how CASPs control mitochondrial function and homeostasis in nonapoptotic scenarios.

In conclusion, our results establish a previously unrecognized role of CASP9 in the promotion of autophagy through maintenance of mitochondrial homeostasis and facilitation of ATG8 conjugation (Figure 12). Elucidation of the cryptic mechanisms underlying CASP9 activation and CASP9-mediated regulation of mitochondrial homeostasis and autophagy will greatly advance our understanding of the autophagy-apoptosis interaction.

Materials and methods

Reagents and antibodies

The following reagents were used: $BafA_1$ (BML-CM110-0100) and Z-VAD-fmk (ALX-260-020-M005) from Enzo Life Sciences; STS (9953) from Cell Signaling Technology; Z-DEVD-fmk (550378) and Z-IETD-fmk (550380) from BD Biosciences; Z-VEID-fmk (FMK006) and Z-LEHD-fmk (FMK008) from R&D Systems; MitoTracker Green FM (M7514), MitoTracker Deep Red FM (M22426), MitoSox Red (M36008), CM-H_2DCFDA (C6827), and TMRE (T669) from Thermo Fisher Scientific. Antibodies against the following proteins were used: MAP1LC3B (NB100-2220), ATG5 (NB110-53818), and APAF1 (NBP1-76999) from Novus Biologicals; GABARAPL1 (11010-1-AP) and GABARAPL2 (18724-1-AP) from Proteintech; FLAG (F3165) from Sigma-Aldrich; GABARAP (13733S), p-MTOR S2448 (5536), MTOR (2972S), p-ULK1 S757 (14202), ULK1 (8054S), BECN1 (3738S), ATG3 (3415), ATG7 (8558), ATG16L1 (8089), pro-CASP3 (9662), cleaved CASP3 (9661), CASP9 (9508), cleaved CASP9 (9595 for human, 9507 for rat), PARP1 (9542), TUBB (2146), VDAC (4866), p-DNM1L S616 (4494), and MFN2 (9482) from Cell Signaling Technology; p-BECN1 S15 (254515) from Abbiotec; p-DNM1L S637 (orb 127984) from Biorbyt; RAB7 (sc-376362), DNM1L (sc-32898), MFN1 (sc-166644) and horseradish peroxidase-conjugated ACTB/β-actin (sc-47778) from Santa Cruz Biotechnology.

Cell cultures

HCN cells derived from the hippocampus of 8-week-old Sprague Dawley rats were cultured in poly-L-ornithine- and laminin-coated tissue culture dishes, as previously described

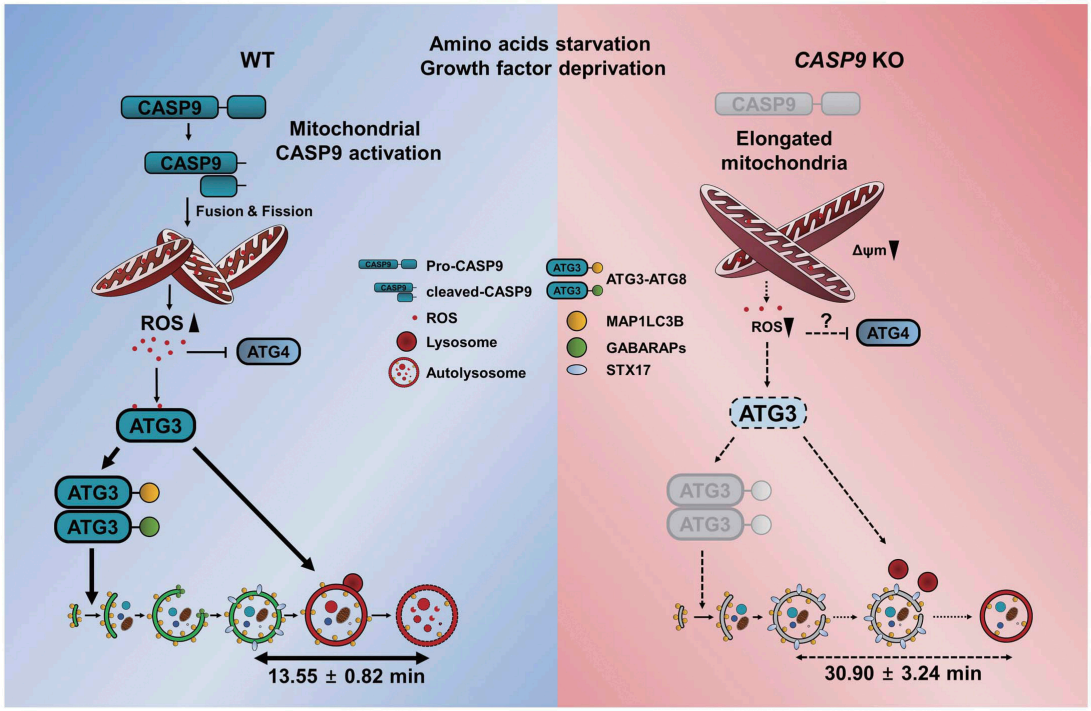

Figure 12. A schematic diagram suggesting that mitochondrial homeostasis and autophagosome maturation requires CASP9. Autophagosome membrane closure and maturation are suppressed due to decreased mitochondrial ROS production in *CASP9* KO cells.

[20]. Cells were maintained in chemically defined serum-free medium containing Dulbecco's modified Eagle's medium (DMEM)/F-12 (Gibco, 12400–024) supplemented with N2 components and basic fibroblast growth factor (20 ng/ml; Peprotech, 100-18B-500). INS was omitted to prepare INS-deficient medium.

HeLa cells were maintained in DMEM containing 10% heat-inactivated fetal bovine serum (Hyclone, SH30084.03) and 1% penicillin–streptomycin (Corning, 30-002-CI). For AA starvation, cells were washed with phosphate-buffered saline (PBS; 137 mM NaCl, 2.7 mM KCl, 4.3 mM Na_2HPO_4, 1.4 mM KH_2PO_4, pH 7.4) twice and then incubated with Earle's balanced salt solution (EBSS) (Sigma, E2888-500ML) for different time periods as indicated in figure legends.

Construction of CRISPR-Cas9 mediated KO cells

sgRNAs for CRISPR-Cas9 mediated gene KO of both rat and human *CASP9*, rat *Apaf1*, and human *ATG3* were designed by and purchased from ToolGen (Republic of Korea). HCN or HeLa cells were transfected with Cas9- and gRNA-encoding plasmids using the Lipofectamine 2000 transfection reagent (Invitrogen, 11688019) according to the manufacturer's protocol. *CASP9*, *APAF1* and *ATG3* KO cells were selected by hygromycin B (Enzo Life Sciences, ALX-380-306-G001) at a concentration of 300 μg/ml for 24 h followed by single-cell colony isolation on a 96-well plate. sgRNA sequences were as follows: for human *CASP9*, 5′-GAACAGCTCGCGGCTCAGCAGGG-3′; for rat *Casp9*, 5′-CTCTGGGTCTCGGCGGGATCAGG-3′; for rat *Apaf1*, 5′-TATGTTGAAGCAAACAATTTCGG-3′.; for human *ATG3*. 5′-TTATAGTGCCGTGCTATAAG-3′.

Cell death assay

Cells were seeded in a 96-well plate at a density of 5×10^4 cells for HCN cells or $2\ 5 \times 10^4$ cells for HeLa cells per cm^2. Cell death was measured by co-staining with Hoechst 33342 (Invitrogen, H3570) and propidium iodide (PI; Sigma-Aldrich, P4170). Images of stained cells were captured using a fluorescence microscope (Axiovert 40 CFL; Carl Zeiss) and Hoechst-positive and PI-positive cells were counted using NIH ImageJ software. Cell death rate (%) calculated as (PI-positive [dead] cell number/Hoechst-positive [total] cell number) × 100.

Subcellular fractionation

Subcellular fractionation was performed as previously described [56]. In brief, HeLa cells were centrifuged at 800 × g for 10 min and then homogenized by Dounce homogenizer for 150 times in STM buffer (250 mM sucrose [Duchefa Biochemie, S0809.1000], 50 mM Tris-HCl, pH 7.4, 5 mM $MgCl_2$, 1 × Halt protease and phosphatase inhibitor cocktail [Thermo Fisher Scientific, 78444]) and kept on ice for 30 min. The homogenate was then mixed by vortexing for 15 s and centrifuged at 800 × g for 15 min and the supernatant (S0) was further centrifuged at 11,000 × g for 10 min twice to separate the supernatant (S2) and pellet (P2). An equal volume of cold 100% acetone was added to S2 and the samples were incubated for at least 1 h at – 20°C to precipitate the proteins. After centrifugation at 12,000 × g for 5 min, the pellet was resuspended in STM + RIPA (Thermo Fisher Scientific, 89901) (1:1) buffer and used as the cytosolic fraction. P2, which contained the mitochondrial fraction, was resuspended in STM buffer and centrifuged at 11,000 × g

for 10 min; the pellet (P3) was washed with STM buffer and centrifuged at 11,000 × g for 10 min. Pellet (P4) was resuspended in STM buffer + RIPA (1:1) and sonicated with a Bioruptor KRB-01 (CosmoBio, Tokyo, Japan) on ice 3 times for 10 s with 30 s intervals. Samples were quantified by BCA protein assay kit. S2 was used as cytosolic fraction and P4 was used as mito fraction, respectively.

Western blotting analysis

Western blotting analysis was performed as previously described [57]. In brief, cell pellets were lysed on ice in radioimmunoprecipitation assay buffer (Thermo Fisher Scientific, 89900) containing 1× protease and phosphatase inhibitors cocktails (Thermo Fisher Scientific, 78444) for 30 min. After incubation, lysates were centrifuged at 12,000 × *g* for 15 min, and protein concentration was measured by using a BCA protein assay kit (Thermo Fisher Scientific, 23224). For non-reducing samples, cells were directly lysed with diluted 4× Laemmli buffer (Bio-Rad, 161–0747) containing protease and phosphatase inhibitor cocktails without dithiothreitol or β-mercaptoethanol (Sigma-Aldrich, M6250-250ML) into plate. Protein samples were heated for 5 min, separated by electrophoresis and transferred onto polyvinylidene fluoride membrane (Merck Millipore, IPVH00010) in a semi-dry electrophoretic transfer cell (Bio-Rad). The membranes were incubated for 1 h at room temperature in a blocking buffer containing 5% skim milk (Sigma-Aldrich, 70166) and 0.1% Tween 20 (Duchefa, P1362.0500) in Tris-buffered saline (TBST). The membranes were then incubated overnight at 4°C with appropriate primary antibodies diluted in TBST containing 5% bovine serum albumin (Thermo Scientific, AAJ1085736) and 0.01% sodium azide (Sigma-Aldrich, S2002). The membranes were washed three times with TBST for 10 min each, followed by 1 h incubation at room temperature with peroxidase-conjugated secondary antibodies diluted in blocking solution. After washing, the membranes were then processed for analysis using a chemiluminescence detection kit (Thermo Fisher Scientific, 34580). Western blots were quantified by ImageJ (NIH) software and normalized to ACTB.

CASP activity assay

CASP9 (Promega, G8210) and CASP3 (Promega, G8090) activity assay kits were used according to the manufacturer's instructions. Cells were seeded onto 96-well white plates at a density of 2×10^4 cells per well. CASP9 and CASP3 Glo reagent solutions were freshly prepared and added to each well and luminescence was recorded using a SpectraMax L luminometer (Molecular Devices). Wells containing medium without cells were used as blank. The luminescence values were normalized by the protein concentration for each condition after blank values were subtracted.

Immunocytochemistry

Cells were fixed with 4% paraformaldehyde (Sigma-Aldrich, P6148-500G) and permeabilized with 0.1% Triton X-100 (Sigma, X100-500ML) in PBS. Cells were blocked with 0.5% bovine serum albumin and incubated overnight with primary antibodies at 4°C, followed by incubation with donkey anti-mouse Alexa Fluor 488 or donkey anti-rabbit Alexa Fluor 647 secondary antibodies (Jackson ImmunoResearch, 715-545-150, 711-605-152). Nuclei were stained with Hoechst 33342. Images were captured using an LSM 780 confocal microscope (Carl Zeiss) or SR-SIM (Carl Zeiss) for STX17 detection, and analyzed by ZEN software (Carl Zeiss).

Live cell imaging

Cells were transfected with GFP-STX17 or DsRed-Mito expression vectors for 24 h and then seeded on an 18 mm cover slip at a density of 1×10^5 cells per well. For detection of GFP-STX17, sgCon and sg*CASP9* HeLa cells were AA-starved, and *z*-stacked images (0.5 μm intervals × 5) were captured at 30 s intervals for 30 min in live imaging chamber supplemented with 5% CO_2 at 37°C. For analysis of mitochondrial dynamics, *z*-stacked (0.5 μm intervals × 5) DsRed-Mito images of sgCon and sg*CASP9* HeLa cells were captured at 5 s intervals for 10 min. For analysis of mitochondrial morphology, *z*-stacked images (0.25 μm intervals × 10) of sgCon and sg*CASP9* cells were captured after 15 min staining with MitoTracker Green with a live imaging confocal microscope (LSM 7, Carl Zeiss).

Quantitative real-time PCR

Total RNA was isolated from cells using the ImProm-II Reverse Transcriptase kit (Promega, A3800) and reverse-transcribed into cDNA as previously described [57]. Quantitative real-time PCR was performed with the CFX96 Real-Time System (Bio-Rad) and iTaq Universal SYBR Green Supermix (Bio-Rad, 1725121). Results were analyzed using CFX96 Manager. *ACTB* (for HeLa) or *Actb* (for HCN) was used as a reference gene for normalization. Primers were as follows: *Atg3* (rat), forward (5′-GCTATGATGAGCAACGGCAGCC-3′) and reverse (5′-ACTTCAGCATGCCTGCAGGGGT-3′); *ATG3* (human), forward (5′- GCTATGATGAGCAACGGCAGCC-3′) and reverse (5′-ACCTCAGCATGCCTGCATGGGT-3′); *ACTB* (human), forward (5′- CCATCCTGCGTCTGGACCTGG-3′) and reverse (5′- TTGCCAATGGTGATGACCTGGCC-3′); *Actb* (rat), forward (5′- CCATCCTGCGTCTGGACCTGG-3′) and reverse (5′- TTGCCGATAGTGATGACCTGA-3′).

PCR cloning of rat casp9 and human ATG3

Rat *Casp9* construct was generated by using Pfu-X polymerase (Solgent, SPX16-R250) from total cDNA of HCN cells. PCR product of *Casp9* was introduced into the pcDNA3.1-HA vector (Addgene, 128034, deposited by Oskar Laur) by *EcoRI* and *NotI* restriction. To generate the C325A mutation, TGT (C325) was changed to GCT (A325). Point mutations were introduced by PCR using Pfu-X polymerase with mutation-containing primers followed by treatment with Dpn1 for 1 h at 37°C. The PCR product was then transformed into DH5α competent *Escherichia coli* cells (RBC, RH617). Human *ATG3* construct was generated from human cDNA library. PCR product of *ATG3* was introduced into the 3× FLAG-

tagged pcDNA-3.1(+) (Invitrogen, V79020; for FLAG tag, 3× FLAG oligomer was introduced by *Kpn1* and *BamH1* restriction) vector by *Eco*RI and *Not*I restriction. All constructs were validated by sequencing.

Fluorescence-activated cell sorting (FACS) analysis

To detect apoptotic cells, HCN cells were seeded in a 24-well plate and INS was removed by changing medium to INS-deficient medium. The cells were treated with STS for different time periods as indicated in figure legends. After treatment, cells were harvested using 0.05% trypsin-EDTA (TE) solution (Hyclone, SH30236.01) and stained for 15 min using a FITC-ANXA5 apoptosis detection kit I (BD Biosciences, 556547) according to the manufacturer's instructions. To measure Δψm, sgCon and sg*CASP9* HeLa cells were treated as described above, harvested using TE, and stained with both MitoTracker Green and MitoTracker Deep Red (100 nM each) for 15 min. To measure intracellular or mitochondrial ROS, cells were harvested using TE, and stained with CM-H_2DCFDA (200 nM) or MitoSox Red (5 μM), respectively. All stained cells were analyzed with an Accuri C6 flow cytometer (BD Biosciences). Non-stained cells were used as a negative control and single-stained cells were used for channel compensation (ANXA5 and MitoTracker Green or MitoTracker Deep Red).

Transfection and expression vectors

GFP-DFCP1 (38269, deposited by Noboru Mizushima), GFP-STX17 (45909, deposited by Noboru Mizushima), DsRed-Mito (55838, deposited by Michael Davidson), and ptfLC3 (encoding mRFP-GFP-MAP1LC3B, 21074, deposited by Tamotsu Yoshimori) were purchased from Addgene. EV-IRES-mCherry and DN-DRP1-IRES-mCherry were kindly provided from Bongki Cho at DGIST. All constructs were validated by sequencing. Transfection of plasmids was performed with Lipofectamine 2000 according to the manufacturer's instructions. Four hours after transfection, medium containing the plasmid-Lipofectamine 2000 mixture was changed to fresh medium, and cells were incubated for another 24 h. Transfected cells were then used for cell death assay, western blotting analysis, or fluorescence imaging.

Alignment of CASP9 isoform sequences

Sequences of human CASP9 isoforms 1, 2, 3, and 4 were aligned using the Multalin website [58].

Statistical analysis

All data are represented as mean ± standard error of the mean (SEM) with at least 3 individual experiments. Statistical analysis was performed using unpaired Student's *t*-test or one-way analysis of variance (ANOVA), and statistical significance (*P* value) was calculated in GraphPad Prism 5 (GraphPad Software). Results were considered significant at the 95% confidence level.

Disclosure statement

No potential conflict of interest was reported by the authors.

Funding

This work was supported by the National Research Foundation of Korea (NRF) grant (2018M3C7A1056275), the DGIST Convergence Science Center Program (19-BD-04), and KBRI basic research program (19-BR-01-08) of the Ministry of Science and ICT of Korea.

ORCID

Ji Young Mun http://orcid.org/0000-0003-0820-6233

References

[1] Klionsky DJ, Emr SD. Autophagy as a regulated pathway of cellular degradation. Science. 2000;290(5497):1717–1721.
[2] Mizushima N, Levine B, Cuervo AM, et al. Autophagy fights disease through cellular self-digestion [Review Article]. Nature. 2008;451:1069. 02/28/online. .
[3] He C, Klionsky DJ. Regulation mechanisms and signaling pathways of autophagy. Annu Rev Genet. 2009;43:67–93.
[4] Klionsky DJ, Abeliovich H, Agostinis P, et al. Guidelines for the use and interpretation of assays for monitoring autophagy in higher eukaryotes. Autophagy. 2008;4(2):151–175.
[5] Mizushima N. Autophagy: process and function. Genes Dev. 2007;21(22):2861–2873.
[6] Mizushima N, Yoshimori T, Ohsumi Y. The role of Atg proteins in autophagosome formation. Annu Rev Cell Dev Biol. 2011;27:107–132.
[7] Lee Y-K, Lee J-A. Role of the mammalian ATG8/LC3 family in autophagy: differential and compensatory roles in the spatiotemporal regulation of autophagy. BMB Rep. 2016;49(8):424.
[8] Pattingre S, Tassa A, Qu X, et al. Bcl-2 antiapoptotic proteins inhibit Beclin 1-dependent autophagy. Cell. 2005;122(6):927–939.
[9] Rubinstein AD, Eisenstein M, Ber Y, et al. The autophagy protein Atg12 associates with antiapoptotic Bcl-2 family members to promote mitochondrial apoptosis. Mol Cell. 2011;44(5):698–709.
[10] Boatright KM, Salvesen GS. Mechanisms of caspase activation. Curr Opin Cell Biol. 2003;15(6):725–731.
[11] Hou Y-C-C, Chittaranjan S, Barbosa SG, et al. Effector caspase Dcp-1 and IAP protein Bruce regulate starvation-induced autophagy during Drosophila melanogaster oogenesis. J Cell Biol. 2008;182(6):1127–1139.
[12] Berry DL, Baehrecke EH. Growth arrest and autophagy are required for salivary gland cell degradation in Drosophila. Cell. 2007;131(6):1137–1148.
[13] DeVorkin L, Go NE, Hou Y-C-C, et al. The Drosophila effector caspase Dcp-1 regulates mitochondrial dynamics and autophagic flux via SesB. J Cell Biol. 2014;205(4):477–492.
[14] Han J, Hou W, Goldstein LA, et al. A complex between Atg7 and caspase-9: a novel mechanism of cross-regulation between autophagy and apoptosis. J Biol Chem. 2013;289:6485–6497. jbc. M113. 536854.
[15] Jeong H-S, Choi HY, Lee E-R, et al. Involvement of caspase-9 in autophagy-mediated cell survival pathway. Biochim Biophys Acta-Mol Cell Res. 2011;1813(1):80–90.
[16] Bell BD, Leverrier S, Weist BM, et al. FADD and caspase-8 control the outcome of autophagic signaling in proliferating T cells. Proc Nat Acad Sci. 2008;105(43):16677–16682.
[17] Tiwari M, Sharma LK, Vanegas D, et al. A nonapoptotic role for CASP2/caspase 2: modulation of autophagy. Autophagy. 2014;10(6):1054–1070.
[18] Norman JM, Cohen GM, Bampton ET. The in vitro cleavage of the hAtg proteins by cell death proteases. Autophagy. 2010;6(8):1042–1056.

[19] Hou W, Han J, Lu C, et al. Autophagic degradation of active caspase-8: a crosstalk mechanism between autophagy and apoptosis. Autophagy. 2010;6(7):891–900.
[20] Chung KM, Park H, Jung S, et al. Calpain determines the propensity of adult Hippocampal neural stem cells to autophagic cell death following insulin withdrawal. Stem Cells. 2015;33 (10):3052–3064.
[21] Yeo BK, Hong CJ, Chung KM, et al. Valosin containing protein is a key mediator between autophagic cell death and apoptosis in adult hippocampal neural stem cells following insulin withdrawal. Mol Brain. 2016;9(1):31.
[22] Ha S, Ryu HY, Chung KM, et al. Regulation of autophagic cell death by glycogen synthase kinase-3β in adult hippocampal neural stem cells following insulin withdrawal. Mol Brain. 2015;8(1):30.
[23] Yu SW, Baek SH, Brennan RT, et al. Autophagic death of adult hippocampal neural stem cells following insulin withdrawal. Stem Cells. 2008;26(10):2602–2610.
[24] Shen H-M, Codogno P. Autophagic cell death: loch Ness monster or endangered species? Autophagy. 2011;7(5):457–465.
[25] Klionsky DJ, Abdelmohsen K, Abe A, et al. Guidelines for the use and interpretation of assays for monitoring autophagy. Autophagy. 2016;12(1):1–222.
[26] Ryu JR, Hong CJ, Kim JY, et al. Control of adult neurogenesis by programmed cell death in the mammalian brain. Mol Brain. 2016;9(1):43.
[27] Wang P, Shi T, Ma D. Cloning of a novel human caspase-9 splice variant containing only the CARD domain. Life Sci. 2006;79 (10):934–940.
[28] Srinivasula SM, Ahmad M, Guo Y, et al. Identification of an endogenous dominant-negative short isoform of caspase-9 that can regulate apoptosis. Cancer Res. 1999;59(5):999–1002.
[29] Ota T, Suzuki Y, Nishikawa T, et al. Complete sequencing and characterization of 21,243 full-length human cDNAs. Nat Genet. 2004;36(1):40.
[30] Li P, Nijhawan D, Budihardjo I, et al. Cytochrome c and dATP-dependent formation of Apaf-1/caspase-9 complex initiates an apoptotic protease cascade. Cell. 1997;91(4):479–489.
[31] Rodriguez J, Lazebnik Y. Caspase-9 and APAF-1 form an active holoenzyme. Genes Dev. 1999;13(24):3179–3184.
[32] Lamb CA, Yoshimori T, Tooze SA. The autophagosome: origins unknown, biogenesis complex. Nat Rev Mol Cell Biol. 2013;14(12):759.
[33] Kim J, Kundu M, Viollet B, et al. AMPK and mTOR regulate autophagy through direct phosphorylation of Ulk1. Nat Cell Biol. 2011;13(2):132.
[34] Russell RC, Tian Y, Yuan H, et al. ULK1 induces autophagy by phosphorylating Beclin-1 and activating VPS34 lipid kinase. Nat Cell Biol. 2013;15(7):741.
[35] Sekulić A, Hudson CC, Homme JL, et al. A direct linkage between the phosphoinositide 3-kinase-AKT signaling pathway and the mammalian target of rapamycin in mitogen-stimulated and transformed cells. Cancer Res. 2000;60(13):3504–3513.
[36] Jung CH, Ro S-H, Cao J, et al. mTOR regulation of autophagy. FEBS Lett. 2010;584(7):1287–1295.
[37] Funderburk SF, Wang QJ, Yue Z. The Beclin 1–VPS34 complex–at the crossroads of autophagy and beyond. Trends Cell Biol. 2010;20(6):355–362.
[38] Axe EL, Walker SA, Manifava M, et al. Autophagosome formation from membrane compartments enriched in phosphatidylinositol 3-phosphate and dynamically connected to the endoplasmic reticulum. J Cell Biol. 2008;182(4):685–701.
[39] Weidberg H, Shvets E, Shpilka T, et al. LC3 and GATE-16/GABARAP subfamilies are both essential yet act differently in autophagosome biogenesis. Embo J. 2010;29(11):1792–1802.
[40] Tsuboyama K, Koyama-Honda I, Sakamaki Y, et al. The ATG conjugation systems are important for degradation of the inner autophagosomal membrane. Science. 2016;354(6315):1036–1041.
[41] Jäger S, Bucci C, Tanida I, et al. Role for Rab7 in maturation of late autophagic vacuoles. J Cell Sci. 2004;117(20):4837–4848.
[42] Eskelinen E-L. Maturation of autophagic vacuoles in mammalian cells. Autophagy. 2005;1(1):1–10.
[43] Dewaele M, Maes H, Agostinis P. ROS-mediated mechanisms of autophagy stimulation and their relevance in cancer therapy. Autophagy. 2010;6(7):838–854.
[44] Scherz-Shouval R, Shvets E, Fass E, et al. Reactive oxygen species are essential for autophagy and specifically regulate the activity of Atg4. Embo J. 2007;26(7):1749–1760.
[45] Li L, Chen Y, Gibson SB. Starvation-induced autophagy is regulated by mitochondrial reactive oxygen species leading to AMPK activation. Cell Signal. 2013;25(1):50–65.
[46] Chen Y, Azad M, Gibson S. Superoxide is the major reactive oxygen species regulating autophagy. Cell Death Differ. 2009;16(7):1040.
[47] Frudd K, Burgoyne T, Burgoyne JR. Oxidation of Atg3 and Atg7 mediates inhibition of autophagy. Nat Commun. 2018;9(1):95.
[48] Karbowski M, Youle R. Dynamics of mitochondrial morphology in healthy cells and during apoptosis. Cell Death Differ. 2003;10(8):870.
[49] Uchiumi F, Watanabe T, Ohta R, et al. PARP1 gene expression is downregulated by knockdown of PARG gene. Oncol Rep. 2013;29 (5):1683–1688.
[50] Kauffman KJ, Yu S, Jin J, et al. Delipidation of mammalian Atg8-family proteins by each of the four ATG4 proteases. Autophagy. 2018;14:1–19.
[51] Kumanomidou T, Mizushima T, Komatsu M, et al. The crystal structure of human Atg4b, a processing and de-conjugating enzyme for autophagosome-forming modifiers. J Mol Biol. 2006;355(4):612–618.
[52] Laussmann MA, Passante E, Düssmann H, et al. Proteasome inhibition can induce an autophagy-dependent apical activation of caspase-8. Cell Death Differ. 2011;18(10):1584.
[53] Young M, Takahashi Y, Khan O, et al. Autophagosomal membrane serves as a platform for an intracellular death-inducing signaling complex (iDISC)-mediated caspase-8 activation and apoptosis. J Biol Chem. 2012;287:12455–12468. jbc. M111. 309104.
[54] Danial NN, Korsmeyer SJ. Cell death: critical control points. Cell. 2004;116(2):205–219.
[55] Chen M, Guerrero AD, Huang L, et al. Caspase-9-induced mitochondrial disruption through cleavage of anti-apoptotic BCL-2 family members. J Biol Chem. 2007;282(46):33888–33895.
[56] Park H, Chung KM, An H-K, et al. Parkin Promotes Mitophagic Cell Death in Adult Hippocampal Neural Stem Cells Following Insulin Withdrawal. Front Mol Neurosci. 2019;12:46.
[57] Chung KM, Jeong E-J, Park H, et al. Mediation of autophagic cell death by type 3 ryanodine receptor (RyR3) in adult hippocampal neural stem cells. Front Cell Neurosci. 2016;10:116.
[58] Corpet F. Multiple sequence alignment with hierarchical clustering. Nucleic Acids Res. 1988;16(22):10881–10890.